

HESSIAN-FREE RAY-BORN INVERSION FOR QUANTITATIVE ULTRASOUND TOMOGRAPHY

ASHKAN JAVAHERIAN

Department of Medical Physics and Biomedical Engineering, University College London, London, UK. WC1E 6BT

ABSTRACT. This study proposes a Hessian-free ray-born inversion approach for biomedical ultrasound tomography. The proposed approach is a more efficient version of the ray-born inversion approach proposed in [3]. Using these approaches, the propagation of acoustic waves are modelled using a ray approximation to heterogeneous Green's function, and the inverse problem is solved in the frequency domain via iteratively linearisation and minimisation of the objective function from low to high frequencies. In [3], the linear subproblem associated with each frequency set is solved via an implicit and iterative inversion of the Hessian matrix (inner iterations). Instead, in this study, each linear subproblem is weighted in a way in which the Hessian matrix be diagonalised, and can thus be inverted in a single step. Using this Hessian-free approach, the computational cost for solving each linear subproblem becomes almost the same as solving one linear subproblem associated with a radon-type time-of-flight-based approach using bent rays. This computational cost is about an order of magnitude less than the equivalent Hessian-based approach proposed in [3]. More importantly, the assumptions made for diagonalising the Hessian matrix make the image reconstruction more robust than the inversion approach in [3] to noise or initial guess.

1. INTRODUCTION

Ultrasound tomography (UST) is a determination of maps of acoustic properties of interior of an object from ultrasonic excitations and measurements done outside the object. Ultrasound tomography has received growing interest for biomedical diagnostic applications [4, 5, 6]. One of the most important application of UST for medical diagnosis is detection of malignant tumours in the breast [4, 7, 8, 9, 10]. Ideally, the information which can be determined from ultrasound data measured outside an object include quantitative distributions of the sound speed, absorption and density, and a qualitative map of reflectivity [6]. This manuscript is concentrated on reconstruction of the sound speed, so the term UST is used for the sound speed reconstruction. Approaches to image reconstruction of the sound speed from UST data can be categorised by: 1) the data type used in the inversion, 2) whether the objective function to be minimised is nonlinear or linearised, 3) whether the objective function is defined in the time domain or frequency domain, or 4) the forward model used.

In terms of the data type used, the first class of approaches use only the direct times-of-flight data between emitters and receivers [11], and no scattered waves are included. The second uses the complete measured time series, including the scattered waves [12, 13, 14, 15, 16, 17]. The third

E-mail address: `ashkan.jawaherian@ut.ac.ir`.

Date: May 2024.

Ashkan Javaherian, Ray-based quantitative-ultrasound toolbox, 2022, <https://github.com/Ash1362/ray-based-quantitative-ultrasound-tomography/>

uses the direct-arrivals and first-scattered waves [18, 19, 20, 21, 36, 23, 24, 25, 26, 27]. In our study, the first and third data types are used, the former for providing an initial guess and the latter for solving the main inverse problem. The chosen approach for solving the main inverse problem is based on an iterative linearisation of the objective function, and performs the linearisations in the frequency domain from low to high frequencies. The forward problem is modelled based on a ray-approximation to heterogeneous Green's function. The motivation for choosing this forward model is that ray theory, which is based on a high frequency approximation, provides a good trade-off between accuracy and computational cost when data is broadband [28]. Compared to seismic imaging applications with sharp changes, the well-known limitations of ray theory such as caustics or mutivaluedness of the minimal acoustic length [29] are less challenging for imaging soft tissues like the breast with refractive index often varying between 0.9 – 1.1. The computational cost and problems with directivity of transducers are the two main challenges for an extension of high-resolution quantitative ultrasound using full-wave inversion to three dimensions, but they can be dealt with using ray-based methods more easily [3]. The details of the proposed UST inversion approach were given in [3]. It was numerically shown that this ray-based approach can reconstruct a high resolution map of the sound speed, but it is computationally a few orders of magnitude less costly than a full-waveform inversion approach which uses the full solution of the wave equation [14, 17].

The common approaches accounting for diffraction or singly scattered waves use the Green's function in the homogeneous medium, and include the acoustic heterogeneity only in the scattering potential [18, 19, 20, 21, 36, 23, 24, 27], but it was shown that combining ray theory with Born inversion can significantly improve the accuracy via including the sound speed heterogeneity, refraction and acoustic absorption and dispersion in the Green's functions predicting the incident and scattered waves [3]. In [30], a one-step inversion approach which combines diffraction tomography with ray tracing was proposed. Using this approach, phase aberration of the Green's function because of heterogeneities was accounted for by performing ray tracing on a low-resolution image reconstructed using a time-of-flight-based approach.

The UST inversion approach proposed in [3] fits into a class of linearised inversion approaches, known as ray-born migration/inversion, in the context of inverse seismic theory [28, 31, 32, 33]. In [3], the objective function is discretised in the frequency domain, and is linearised and minimised over the frequency range covered by ultrasound transducers. This is done by dividing the frequency range into a number of frequency intervals, each including a fixed number, here 2, of the discretised frequencies, and performing the minimisation sequentially from low to high frequency sets such that the solution of the linearised subproblem associated with each frequency set is used as an initial guess for the linearised subproblem corresponding to the next frequency set. Because reconstructing acoustic parameters from ultrasound data is a nonlinear inverse problem, minimising objective function from low to high frequencies helps avoiding getting stuck in the local minima [12, 13, 27]. In [3], each linearised subproblem, which is equivalent to a product of an implicit inverse of the Hessian matrix by gradient of the objective function, is solved using a Conjugate Gradient (CG) algorithm via an iterative computation of the Fréchet derivative of the forward operator and its adjoint. Considering that each iteration is equivalent to a two-way forward propagation using Green's functions initialised on each emitter and scattered on every point in the abject, a two-way back-projection using Green's functions initialised on receivers and scattered on every point in the abject, and then repetition and summation over all emitters, the computational cost for solving each linearised subproblem becomes about an order of magnitude more than solving each linearised subproblem associated with a Radon-type time-of-flight-based approach, for which the system matrix associated with each linearised subproblem can be stored explicitly, because each

time-series is reduced to a scalar representing a time of flight. Hence, the major computational cost associated with a time-of-flight-based approach corresponds to only two-point ray tracing done for constructing the system matrix. Despite a computational cost because of implicitly inverting the Hessian matrix, using the CPU mentioned in section 6.3, the whole computational time for image reconstruction using the ray-born inversion approach in [3] is almost the same as numerically solving a single forward problem for simulating propagation of acoustic waves using a k-space pseudo-spectral approach in a full-waveform inversion framework [35, 36, 37, 38]. This study further reduces the computational cost by proposing a single-stage approach for solving the linearised subproblem associated with each frequency set. The proposed approach is based on weighting each arising linearised subproblem such that the Hessian matrix becomes diagonalised and can thus be inverted in a single step. Using the proposed image reconstruction approach, the computational cost for solving each linearised subproblem is reduced to almost that of a Radon-type time-of-flight-based inversion approach using bent rays [34].

Section 2 introduces a Green's function solution to the frequency-domain Helmholtz wave equation based on ray theory and for heterogeneous and absorbing media. In section 3, the proposed Hessian-free ray-born inversion approach for solving the inverse problem of UST is explained. Section 4 describes ray tracing and how the Green's function for heterogeneous media is approximated based on the ray theory. Section 5 explains the procedure for discretising the forward and inverse problems. In section 6, ray approximation to heterogeneous Green's function is numerically validated, and reconstructed images demonstrating performance of the proposed Hessian-free ray-born inversion approach are presented, and compared to the more costly Hessian-based inversion approach proposed in [3]. A discussion of significance of results follows in section 7.

2. GREEN'S FUNCTION SOLUTION TO THE WAVE EQUATION

This section describes the forward problem of image reconstruction of the sound speed. Let $\mathbf{x} = [x^1, \dots, x^d]^T$ denote a spatial position in \mathbb{R}^d with d the number of dimensions. In general, d can be either 2 or 3. This study is restricted to $d = 2$, but the ultimate purpose is an extension of this study to $d = 3$. Accordingly, $\Omega \subset \mathbb{R}^d$ is an open bounded set, and contains the spatially-varying part of the sound speed distribution, $c(\mathbf{x})$, i.e., $[c_0/c(\mathbf{x}) - 1] \in c_0^\infty$, where c_0 is a scalar value representing the sound speed outside Ω (here the sound speed in water). The open set Ω is bounded by a circular ring $\mathbb{S} \subset \mathbb{R}^{d-1}$, which contains the emission and reception elements \bar{e} and \bar{r} . (The emission and reception elements are assumed points.) Each emission element, referred to here as emitter $\bar{e} \in \{1, \dots, N_e\}$ and centred on position e , is sequentially excited by a pulse and acts as a source $s(t, e)$ within the excitation time $t \in (0, T_s)$. The acoustic pressure field produced by each emitter propagates across the object in water and is measured at the reception elements, referred to here as receivers $\bar{r} \in \{1, \dots, N_r\}$ and centred on positions r , for times $t \in (0, T)$ with $T \gg T_s$. For each excitation element \bar{e} , the time series measured by the receiver \bar{r} is represented by $p(t, r, e)$. The inverse problem is an image reconstruction of $c(x)$ from the measured pressure times series $p(t, r, e)$ for all emitter-receiver pairs, given the source $s(t, e)$.

While the data is typically measured in the time domain, i.e. with a broadband excitation signal, the image reconstruction is here performed in the frequency domain. To this end, we define the following Fourier transform pair between the time and temporal frequency domains,

$$\hat{p}(\omega) = \mathcal{F}p(t) = \int_{-\infty}^{\infty} p(t)e^{i\omega t} dt, \quad p(t) = \mathcal{F}^{-1}\hat{p}(\omega) = \frac{1}{2\pi} \int_{-\infty}^{\infty} \hat{p}(\omega)e^{-i\omega t} d\omega. \quad (1)$$

2.1. Lossy Helmholtz equation and complex wavevector. The propagation of a single frequency acoustic pressure field, $\hat{p}(\omega, \mathbf{x})$, in an absorbing medium is often modelled using a lossy

Helmholtz equation of the form

$$[\tilde{k}(\mathbf{x})^2 + \nabla^2] \hat{p}(\omega, \mathbf{x}, e) = -s(\omega, e), \quad (2)$$

where the specific form of the wavenumber we use is based on Szabo's absorption model, and is in the form [39]

$$\begin{aligned} \tilde{k} &= \frac{\omega}{c} - \frac{\alpha_0(-i)^{y+1}\omega^y}{\cos(\pi y/2)} \\ &= \frac{\omega}{c} + \alpha [\tan(\pi y/2) + i] = k + i\alpha, \end{aligned} \quad (3)$$

where the scalar α is acoustic absorption and follows the frequency power law, $\alpha = \alpha_0\omega^y$. Here, α_0 has units $\text{Np}(\text{rad/s})^{-y}\text{m}^{-1}$, and y is the power-law exponent with a non-integer often in the range $1 < y \leq 1.5$ for soft tissue [40, 41]. In (3), $(-i)^y = \cos(\pi y/2) - i \sin(\pi y/2)$ has been used. Using the specific form (3), the phase speed satisfies

$$\frac{1}{c_p(\omega)} = \frac{k}{\omega} = \frac{1}{c} + \alpha_0 \tan(\pi y/2) \omega^{(y-1)}. \quad (4)$$

For further details, see [39]. The solution of (2) in terms of Green's function can be written as

$$\hat{p}(\omega, \mathbf{x}) = \int g(\omega, \mathbf{x}, \mathbf{x}') s(\omega, \mathbf{x}') d\mathbf{x}', \quad (5)$$

where $g(\omega, \mathbf{x}, \mathbf{x}')$ is the Green's function associated with frequency ω , at point \mathbf{x} and originated at point \mathbf{x}' , and satisfies

$$[\tilde{k}(\mathbf{x})^2 + \nabla^2] g(\omega, \mathbf{x}, \mathbf{x}') = -\delta(\mathbf{x} - \mathbf{x}'). \quad (6)$$

The complex wavevector is defined as $\tilde{\mathbf{k}} = \mathbf{k} + i\mathbf{k}_i$, where the real part \mathbf{k} is related to the phase speed $c_p(\omega)$ of the wave by

$$|\mathbf{k}| \equiv k = \omega/c_p(\omega), \quad (7)$$

and the imaginary part is related to the absorption coefficient α by

$$\mathbf{k}_i = \alpha \mathbf{k}/k. \quad (8)$$

For the 2D case and in heterogeneous and absorbing media, the Green's function associated with frequency ω , at point \mathbf{x} and originated at \mathbf{x}' , can be written in the form

$$g(\omega, \mathbf{x}, \mathbf{x}') \approx A(\omega, \mathbf{x}, \mathbf{x}') \exp\left(i[\phi(\omega, \mathbf{x}, \mathbf{x}') + \pi/4]\right). \quad (9)$$

Here, ϕ is the phase, and $A = A_{abs}A_{geom}$ is the amplitude factor, where A_{abs} and A_{geom} are contributions from absorption and geometric spreading, respectively. Plugging the Green's function 9 into the Helmholtz equation 6, using an assumption $\alpha^2 \ll k^2$, which is valid for soft tissues, and a high-frequency approximation $|\nabla^2 A/A| \ll k^2$, gives *Eikonal* equation

$$\nabla\phi \cdot \nabla\phi = k^2, \quad (10)$$

and *Transport* equation

$$\nabla \cdot [A_{geom}^2 \nabla\phi] = 0. \quad (11)$$

Considering the *Eikonal* equation (10), rays are curves that are perpendicular to surfaces of constant phase, i.e., they are tangent to the complex wavevector's real part, \mathbf{k} , and satisfies

$$\mathbf{k} = \nabla\phi. \quad (12)$$

Having determined rays' trajectories, the accumulated phase is determined by

$$\phi(\mathbf{x}, \mathbf{x}') = \exp \left(\int_{\mathcal{C}(\mathbf{x}, \mathbf{x}')} \mathbf{k} \cdot d\mathbf{x} \right), \quad (13)$$

and the accumulated absorption contribution to the amplitude satisfies

$$A_{abs}(\mathbf{x}, \mathbf{x}') = \exp \left(- \int_{\mathcal{C}(\mathbf{x}, \mathbf{x}')} \mathbf{k}_i \cdot d\mathbf{x} \right). \quad (14)$$

Here, $\mathcal{C}(\mathbf{x}, \mathbf{x}')$ denotes a curve which represents trajectory of a reference ray linking the points \mathbf{x}' and \mathbf{x} , and \mathbf{x} is an arbitrary point on \mathcal{C} . In addition, the *Transport* equation (11) gives a geometrical attenuation which satisfies

$$A_{geom}(\mathbf{x}, \mathbf{x}') = \left[\frac{S(\mathbf{x}') \rho(\mathbf{x}) c(\mathbf{x})}{S(\mathbf{x}) \rho(\mathbf{x}') c(\mathbf{x}')} \right]^{1/2}, \quad (15)$$

where ρ is medium's density and is assumed homogeneous, i.e., $\rho(\mathbf{x}) = \rho(\mathbf{x}')$ for all \mathbf{x} and \mathbf{x}' in Ω . In addition, $S(\mathbf{x})$ stands for area of ray tube on \mathbf{x} , and is determined using a paraxial ray which is approximated in a vicinity of a reference ray satisfying the *Eikonal* equation. By setting $\mathbf{x}' = \mathbf{x}_0$, which is the initial point of the ray, the accumulated phase ϕ and acoustic absorption A_{abs} can be determined along the reference rays initialised on \mathbf{x}_0 using Eqs. (13) and (14), respectively. However, by setting $\mathbf{x}' = \mathbf{x}_0$ in Eq. (15), $A_{geom}(\mathbf{x}, \mathbf{x}_0)$ will vanish, because area of ray tube is zero on the initial point \mathbf{x}_0 [29]. Therefore, the geometrical contribution to amplitude is determined with respect to a reference point \mathbf{x}_{ref} on the ray with $|\mathbf{x}_{ref} - \mathbf{x}_0| < \varepsilon$, where ε is the radius of a small neighborhood of \mathbf{x}_0 in which acoustic properties are assumed homogeneous. Using this homogeneity assumption, the amplitude on the chosen reference point can be calculated analytically using

$$A_{geom}(\mathbf{x}_{ref}, \mathbf{x}_0) = [8\pi\phi(\mathbf{x}_{ref}, \mathbf{x}_0)]^{-1/2}. \quad (16)$$

Given the amplitude on the reference point, the geometrical amplitude on any arbitrary point along the reference ray can be obtained using

$$A_{geom}(\mathbf{x}, \mathbf{x}_0) = A_{geom}(\mathbf{x}_{ref}, \mathbf{x}_0) A_{geom}(\mathbf{x}, \mathbf{x}_{ref}), \quad (17)$$

where $A_{geom}(\mathbf{x}, \mathbf{x}_{ref})$ is determined using Eq. (15) for $\mathbf{x}' = \mathbf{x}_{ref}$. The readers are referred to reference [3], section 3, for further details.

3. MINIMISATION APPROACH

This section explains the proposed approach for solving the nonlinear inverse problem of UST, i.e., a reconstruction of the sound speed distribution c of an object from pressure time series $p(t, r, e)$ collected through sequential excitations and measurements done using an array of ultrasound transducers encompassing the object. Following [3], an associated objective function is linearised at a number of discretised frequencies within the frequency range of the ultrasound transducers, and the arising linearised subproblems are solved from low to high frequencies such the solution for a frequency set is used as initial guess for solving the linearised subproblem associated with the next frequency set. Each linearised subproblem, in its naive form, is equivalent to computing a product of an implicit inverse of the Hessian matrix by gradient of the objective function, and can be solved via iteratively computing products of the Hessian matrix by perturbations to the unknown parameter of interest, the sound speed, until a perturbation which minimises the associated linearised objective function is determined [3]. As an alternative to the iterative approach taken in [3], here, each linearised subproblem is weighted in data and solution spaces so that the Hessian matrix be diagonalised and can thus be inverted in a single step.

In [3], the objective function was minimised in terms of the sound speed c , but here, the objective function is minimised in terms of the squared slowness, $m = 1/c^2$, in order to simplify diagonalisation of the Hessian matrix. Accordingly, a weighted objective function is defined in terms of Green's function in the frequency domain

$$\mathcal{F}(m) = \frac{1}{2} \sum_{e,r} \int \delta g_{res}(m; \omega, r, e)^* \mathcal{Q}_g(m; \omega, r, e) \delta g_{res}(m; \omega, r, e) d\omega, \quad (18)$$

where $*$ denotes the complex conjugate, and $\mathcal{Q}_g(m; \omega, r, e)$ is a component of a diagonal matrix which weights the objective function in data space (ω, r, e) , and will be derived later. Also, δg_{res} is the *residual*, and is in the form

$$\delta g_{res}(m; \omega, r, e) = g(m; \omega, r, e) - \hat{g}(\omega, r, e). \quad (19)$$

Here, $g(m; \omega, r, e)$ and $\hat{g}(\omega, r, e)$ are termed *approximated* and *measured* Green's functions associated with frequency ω , on receiver position r and originated on emitter position e . Note that $\hat{g}(\omega, r, e)$ is obtained by deconvolution of the source $s(\omega, e)$ from the measured pressure $\hat{p}(\omega, r, e)$ in the frequency domain. (The same procedure can be taken directly using an objective function in terms of pressure data [3].)

The n -th linearisation of the objective function (18) around the squared slowness $m^{(n)}$ yields

$$\delta m^{(n)} \approx \arg \min_{\delta m} \frac{1}{2} \sum_{e,r} \int \left[\delta g^{(n)}(\omega, r, e) [\delta m] + \delta g_{res}^{(n)}(\omega, r, e) \right]^* \mathcal{Q}_g^{(n)}(\omega, r, e) \times \left[\delta g^{(n)}(\omega, r, e) [\delta m] + \delta g_{res}^{(n)}(\omega, r, e) \right] d\omega, \quad (20)$$

where \times is a product operator acting on scalars and the notations $\mathcal{Q}_g^{(n)}(\omega, r, e) := \mathcal{Q}_g(m^{(n)}; \omega, r, e)$ and $\delta g_{res}^{(n)}(\omega, r, e) := \delta g_{res}(m^{(n)}; \omega, r, e)$ have been used for brevity, and will be applied from now on. The linearised minimisation subproblem (20) seeks to find a perturbation $\delta m^{(n)}$ which fits a perturbed Green's function on receivers to the minus residual in data space (ω, r, e) . The perturbed Green's function $\delta g^{(n)}(\omega, r, e) [\delta m]$ is in the form

$$\delta g^{(n)}(\omega, r, e) [\delta m] = \int \frac{\partial g^{(n)}(\omega, r, e)}{\partial m^{(n)}(\mathbf{x}')} \delta m(\mathbf{x}') d\mathbf{x}'. \quad (21)$$

Here, the notation $g^{(n)}(\omega, r, e) := g(m^{(n)}; \omega, r, e)$ has been used, and $\partial g^{(n)}(\omega, r, e) / \partial m^{(n)}(\mathbf{x}')$ is a component of Fréchet derivative of the Green's function with respect to the squared slowness m on point \mathbf{x}' . The Fréchet derivative operator linearly acts on the perturbation δm , and its components satisfy

$$\frac{\partial g^{(n)}(\omega, r, e)}{\partial m^{(n)}(\mathbf{x}')} = g^{(n)}(\omega, r, \mathbf{x}') \Upsilon_m^{(n)}(\omega, \mathbf{x}') g^{(n)}(\omega, \mathbf{x}', e), \quad (22)$$

where $g(\omega, \mathbf{x}', e)$ is the Green's function on point \mathbf{x}' and originated on emitter position e , and $g(\omega, r, \mathbf{x}')$ is the Green's function on receiver position r and originated on \mathbf{x}' . Also,

$$\Upsilon_m^{(n)}(\omega, \mathbf{x}') = \Upsilon_c^{(n)}(\omega, \mathbf{x}') \frac{\partial c(\mathbf{x}')}{\partial m(\mathbf{x}')} = \omega c^{(n)}(\mathbf{x}') \tilde{k}^{(n)}(\mathbf{x}') \quad (23)$$

where $\tilde{k}^{(n)}$ satisfies Eq. (3) for $c^{(n)}$ and α . Note that α has been assumed fixed, and is thus not changed with n . (The reader is referred to reference [3], section 4.1, for further details about how

Eq. (22) has been derived.) The linearised minimisation subproblem (20) is equivalent to solving the linear equation

$$\nabla \mathcal{F}^{(n)}(\mathbf{x}) + \int H^{(n)}(\mathbf{x}, \mathbf{x}') \delta m(\mathbf{x}') d\mathbf{x}' = 0. \quad (24)$$

Here, the first term in the left-hand side is the functional gradient, which is here weighted in data space (ω, r, e) and solution space \mathbf{x} , and is in the form

$$\nabla \mathcal{F}^{(n)}(\mathbf{x}) = \sum_{e,r} \int \mathcal{Q}_m^{(n)}(\mathbf{x}) \left[\frac{\partial g^{(n)}(\omega, r, e)}{\partial m^{(n)}(\mathbf{x})} \right]^* \mathcal{Q}_g^{(n)}(\omega, r, e) \delta g_{res}^{(n)}(\omega, r, e) d\omega. \quad (25)$$

Also, the second term is the action of the Hessian matrix, which is weighted in data and solution spaces in the same way, on the perturbation, and is in the form [3]

$$H^{(n)}(\mathbf{x}, \cdot) \delta m = \sum_{e,r} \int \mathcal{Q}_m^{(n)}(\mathbf{x}) \left[\frac{\partial g^{(n)}(\omega, r, e)}{\partial m^{(n)}(\mathbf{x})} \right]^* \mathcal{Q}_g^{(n)}(\omega, r, e) \delta g^{(n)}(\omega, r, e) [\delta m] d\omega. \quad (26)$$

Here, $H^{(n)}(\mathbf{x}, \cdot) \delta m = \int H^{(n)}(\mathbf{x}, \mathbf{x}') \delta m(\mathbf{x}') d\mathbf{x}'$, where from (21) and (22),

$$\delta g^{(n)}(\omega, r, e) [\delta m] = \int g^{(n)}(\omega, r, \mathbf{x}') \Upsilon_m^{(n)}(\omega, \mathbf{x}') \delta m(\mathbf{x}') g^{(n)}(\omega, \mathbf{x}', e) d\mathbf{x}'. \quad (27)$$

Also, $\Upsilon_m^{(n)}(\omega, \mathbf{x}') \delta m(\mathbf{x}')$ is the complex scattering potential on point \mathbf{x}' . By plugging (9) into (26), the weighted Hessian can be written in the explicit form

$$H^{(n)}(\mathbf{x}, \mathbf{x}') = \sum_{e,r} \int \mathcal{Q}^{(n)}(\omega, r, e, \mathbf{x}) \mathcal{D}^{(n)}(\omega, r, e, \mathbf{x}, \mathbf{x}') e^{-i\Phi^{(n)}(\omega, r, e, \mathbf{x}, \mathbf{x}')} d\omega, \quad (28)$$

where

$$\mathcal{Q}^{(n)}(\omega, r, e, \mathbf{x}) = \mathcal{Q}_m^{(n)}(\mathbf{x}) \mathcal{Q}_g^{(n)}(\omega, r, e). \quad (29)$$

Also,

$$\begin{aligned} \mathcal{D}^{(n)}(\omega, r, e, \mathbf{x}, \mathbf{x}') = & \left[A^{(n)}(\omega, r, \mathbf{x}) \Upsilon_m^{(n)}(\omega, \mathbf{x}) A^{(n)}(\omega, \mathbf{x}, e) \right]^* \\ & \left[A^{(n)}(\omega, r, \mathbf{x}') \Upsilon_m^{(n)}(\omega, \mathbf{x}') A^{(n)}(\omega, \mathbf{x}', e) \right], \end{aligned} \quad (30)$$

and

$$\begin{aligned} \Phi^{(n)}(\omega, r, e, \mathbf{x}, \mathbf{x}') = & \phi^{(n)}(\omega, r, \mathbf{x}) + \phi^{(n)}(\omega, \mathbf{x}, e) \\ & - [\phi(\omega, r, \mathbf{x}') + \phi(\omega, \mathbf{x}', e)]. \end{aligned} \quad (31)$$

Now, the following two approximations are enforced on (28) [28, 31, 32, 33].

$$\mathcal{D}^{(n)}(\omega, r, e, \mathbf{x}, \mathbf{x}') \approx \mathcal{D}^{(n)}(\omega, r, e, \mathbf{x}', \mathbf{x}') \quad (32)$$

and

$$\begin{aligned} \Phi^{(n)}(\omega, r, e, \mathbf{x}, \mathbf{x}') \approx & \nabla_{\mathbf{x}'} \left(\phi^{(n)}(\omega, r, \mathbf{x}') + \phi^{(n)}(\omega, \mathbf{x}', e) \right) \cdot (\mathbf{x} - \mathbf{x}') \\ = & \bar{\mathbf{k}}^{(n)}(\omega, r, e, \mathbf{x}) \cdot (\mathbf{x} - \mathbf{x}'). \end{aligned} \quad (33)$$

Here, $\bar{\mathbf{k}}(\omega, r, e, \mathbf{x}')$ is the gradient of a two-way isochron, a curve in the space of the scattering point \mathbf{x}' on which the sum of accumulated phase from emitter position e to the scatterer \mathbf{x}' and from the scatterer \mathbf{x}' to receiver position r is equal [31, 32]. $\bar{\mathbf{k}}(\omega, r, e, \mathbf{x}')$ is thus a vector passing through \mathbf{x}' , normal to the two-way isochron, where $\bar{\mathbf{k}}(\omega, r, e, \mathbf{x}') = \mathbf{k}(\omega, \mathbf{x}', e) + \mathbf{k}(\omega, r, \mathbf{x}') = \mathbf{k}(\omega, \mathbf{x}', e) -$

$\mathbf{k}(\omega, \mathbf{x}', r)$ with $\mathbf{k}(\omega, \mathbf{x}', e) = \nabla_{\mathbf{x}'} \phi(\omega, \mathbf{x}', e)$ (resp. $\mathbf{k}(\omega, \mathbf{x}', r) = \nabla_{\mathbf{x}'} \phi(\omega, \mathbf{x}', r)$) the wavevector of the ray initialised on emitter position e (resp. receiver position r) and on point \mathbf{x}' .

For sufficiently smooth wavenumber field k , the contribution of e and r to the Hessian $H(\mathbf{x}, \mathbf{x}')$ oscillates by moving far away from a ray linking the emitter-receiver positions (e, r) along the planes perpendicular to the ray and vanishes everywhere except in some vicinity of the ray. By moving far away from the linked ray, $\Phi^{(n)}(\omega, r, e, \mathbf{x}, \mathbf{x}')$ oscillates and $\mathcal{D}^{(n)}(\omega, r, e, \mathbf{x}, \mathbf{x}')$ decreases, and therefore the contribution of e and r to the Hessian decays. In ray theory, for any emission point e and reception point r , the volume around a ray linking e and r that contributes into the wavefield on r has been widely studied, and is termed *Fresnel volume*. A point \mathbf{x} belongs to the Fresnel volume corresponding to a ray linking positions (e, r) at frequency ω , if and only if the discrepancy of the accumulated phase on the ray linking e and r and the sum of accumulated phase from e to \mathbf{x} and \mathbf{x} to r be smaller than π rad, i.e.,

$$|\phi(\omega, r, \mathbf{x}) + \phi(\omega, \mathbf{x}, e) - \phi(\omega, r, e)| < \pi. \quad (34)$$

For further details, the reader is referred to reference [29], section 3.1.6. By assuming that rays do not have any caustics, only points which are sufficiently close to the ray linking e and r satisfy (34). This assumption holds well for soft tissues. The approximation (33) implies that for any pair of points \mathbf{x} and \mathbf{x}' with sufficiently small $|\phi(\omega, r, \mathbf{x}) + \phi(\omega, \mathbf{x}, e) - \phi(\omega, r, e)|$, the two-way accumulated phase associated with \mathbf{x} can be approximated using a Taylor-series expansion to the two-way accumulated phase associated with \mathbf{x}' , for which the second and higher-order terms are neglected. In addition, the approximation (32) assumes that for any pair of points \mathbf{x} and \mathbf{x}' in some vicinity of the ray linking e and r ,

$$A(\omega, r, \mathbf{x}) \Upsilon_m(\omega, \mathbf{x}) A(\omega, \mathbf{x}, e) \approx A(\omega, r, \mathbf{x}') \Upsilon_m(\omega, \mathbf{x}') A(\omega, \mathbf{x}', e). \quad (35)$$

This approximation is based on two assumptions. Firstly, in some vicinity of a linked ray (e, r) that contributes into the Hessian, the changes in the two-way attenuation from e to r are ignored. Secondly, considering (23), it was assumed that the variations in $\alpha_0 c \omega^{(y-1)}$ throughout the medium is much smaller than 1. For example, for soft tissues like the breast, the sound speed 1500 ms^{-1} , $\alpha_0 = 0.5 \text{ dBMHz}^{-y} \text{cm}^{-1}$ (equivalent to $1.75 \times 10^{-9} \text{ Np}(\text{rad/s})^{-y} \text{m}^{-1}$), and frequency 1MHz , will give $\alpha_0 c \omega^{(y-1)} \approx 6.6 \times 10^{-4} \text{ Np/rad}$.

Now, by plugging the approximations (32) and (33) into (28), the Hessian operator is reduced to the form

$$\begin{aligned} H^{(n)}(\mathbf{x}, \mathbf{x}') &= \sum_{e,r} \int \mathcal{Q}^{(n)}(\omega, r, e, \mathbf{x}) e^{-i\bar{\mathbf{k}}^{(n)}(\omega, r, e, \mathbf{x}') \cdot (\mathbf{x} - \mathbf{x}')} \mathcal{D}^{(n)}(\omega, r, e, \mathbf{x}', \mathbf{x}') d\omega \\ &= \iiint \frac{1}{\Delta e \Delta r} \mathcal{Q}^{(n)}(\omega, r, e, \mathbf{x}) e^{-i\bar{\mathbf{k}}^{(n)}(\omega, r, e, \mathbf{x}') \cdot (\mathbf{x} - \mathbf{x}')} \mathcal{D}^{(n)}(\omega, r, e, \mathbf{x}', \mathbf{x}') d\omega dr de. \end{aligned} \quad (36)$$

Now, by assuming that rays do not have caustics or any other singularities, the variables of integration are changed using a one-to-one map $(\omega, r, e) \rightarrow (|\bar{\mathbf{k}}|, \zeta, \theta)$. Here, on each arbitrary point \mathbf{x} , and emitter-receiver positions (e, r) , $\theta(\omega, r, e, \mathbf{x}')$ is defined as the scattering angle, which satisfies

$$\theta(\omega, r, e, \mathbf{x}') = [\gamma(\omega, \mathbf{x}', r) + \pi] - \gamma(\omega, \mathbf{x}', e), \quad (37)$$

where $\gamma(\omega, \mathbf{x}', e)$ (resp. $\gamma(\omega, \mathbf{x}', r)$) is the angle of the wavevector of a ray initialised on e (resp. r). Note that the trajectory of a ray is dependent on ω through the wavenumber field k . Also, note that π rad has been added to $\gamma(\omega, \mathbf{x}', r)$, because the scattered wave is initialised on \mathbf{x}' and travels to r , whereas the corresponding wavevector $\mathbf{k}(\omega, \mathbf{x}', r)$ is initialised on r .

Also, the pair $(|\bar{\mathbf{k}}|, \zeta)$ is a polar representation of a two-way wavevector $\bar{\mathbf{k}}(\omega, r, e, \mathbf{x}')$, which is normal to a two-way isochron associated with the two-way accumulated phase $\phi(\omega, r, \mathbf{x}') + \phi(\omega, \mathbf{x}', e)$. Here,

the angle of the two-way wavevector $\zeta(\omega, r, e, \mathbf{x}')$ satisfies

$$\zeta(\omega, r, e, \mathbf{x}') = \frac{1}{2} [\gamma(\omega, \mathbf{x}', r) + \pi] + \gamma(\omega, \mathbf{x}', e), \quad (38)$$

and the magnitude satisfies

$$|\bar{\mathbf{k}}| = 2 k \cos\left(\frac{\theta}{2}\right). \quad (39)$$

Now, applying a change of variables $(\omega, r, e) \rightarrow (|\bar{\mathbf{k}}|, \zeta, \theta)$ on (36) yields

$$\begin{aligned} H^{(n)}(\mathbf{x}, \mathbf{x}') = \iiint \frac{1}{\Delta e \Delta r} \mathcal{Q}^{(n)}(\omega, r, e, \mathbf{x}) e^{-i\bar{\mathbf{k}}^{(n)}(\omega, r, e, \mathbf{x}') \cdot (\mathbf{x} - \mathbf{x}')} \times \\ \mathcal{D}^{(n)}(\omega, r, e, \mathbf{x}', \mathbf{x}') \left| \frac{\partial(\omega, r, e)}{\partial(|\bar{\mathbf{k}}|, \zeta, \theta)} \right| d|\bar{\mathbf{k}}| d\zeta d\theta, \end{aligned} \quad (40)$$

where \times is a multiplication operator for scalars. Following [28, 31, 32, 33], $\mathcal{Q}^{(n)}$ is now chosen such that $H^{(n)}(\mathbf{x}, \mathbf{x}')$ be diagonalised and can thus be inverted in a single step. Accordingly, by choosing

$$\mathcal{Q}^{(n)}(\omega, r, e, \mathbf{x}) = \frac{\Delta e \Delta r}{(2\pi)^2} \frac{|\bar{\mathbf{k}}^{(n)}(\omega, r, \mathbf{x}; e)|}{\mathcal{D}^{(n)}(\omega, r, e, \mathbf{x}, \mathbf{x})} \left| \frac{\partial(|\bar{\mathbf{k}}|, \zeta, \theta)}{\partial(\omega, r, e)} \right|, \quad (41)$$

the Hessian operator in (40) collapses to

$$H(\mathbf{x}, \mathbf{x}') = \int \left[\frac{1}{(2\pi)^2} \iint |\bar{\mathbf{k}}| e^{-i\bar{\mathbf{k}}(\mathbf{x}') \cdot (\mathbf{x} - \mathbf{x}')} d|\bar{\mathbf{k}}| d\zeta \right] d\theta \approx 2\pi \delta(\mathbf{x} - \mathbf{x}'). \quad (42)$$

Here, we used the fact that the term inside the parenthesis in (42) can be expressed as a sampled (in angular and wavenumber domains) and band-limited variant of the exact Fourier transform of the delta function in the cylindrical coordinates [31], i.e.,

$$\frac{1}{(2\pi)^2} \int_{\zeta=0}^{2\pi} \int_{-\infty}^{+\infty} |\bar{\mathbf{k}}| e^{-i\bar{\mathbf{k}}(\mathbf{x}') \cdot (\mathbf{x} - \mathbf{x}')} d|\bar{\mathbf{k}}| d\zeta = \delta(\mathbf{x} - \mathbf{x}'). \quad (43)$$

In addition, the Jacobian determinant included in the weighting function (41) gives

$$\left| \frac{\partial(|\bar{\mathbf{k}}|, \zeta, \theta)}{\partial(\omega, r, e)} \right| = \left| \frac{\partial \gamma_e}{\partial e} \right| \left| \frac{\partial \gamma_r}{\partial r} \right| \left| \frac{\partial(|\bar{\mathbf{k}}|)}{\partial \omega} \right|, \quad (44)$$

where

$$\frac{\partial(|\bar{\mathbf{k}}(\mathbf{x})|)}{\partial \omega} = 2 \cos\left(\frac{\theta(\mathbf{x})}{2}\right) \left[\frac{1}{c(\mathbf{x})} + y \tan\left(\frac{\pi y}{2}\right) \omega^{(y-1)} \alpha_0(\mathbf{x}) \right]. \quad (45)$$

Now, considering (29) and by plugging the weighting function in (41) into the functional gradient (25), and then plugging (25) into the linearised equation (24), together with using (42), give a search direction

$$\delta m^{(n)}(\mathbf{x}') \approx \Re \left\{ \sum_{e, r, \omega} \Lambda^{(n)}(\omega, r, e, \mathbf{x}') \delta g_{res}(m^{(n)}; \omega, r, e) \right\}. \quad (46)$$

Here, $\Re \{\cdot\}$ denotes the real part, and

$$\begin{aligned} \Lambda^{(n)}(\omega, r, e, \mathbf{x}') = & \frac{\Delta e \Delta r \Delta \omega}{(2\pi)^3} \left| \frac{\partial \gamma^{(n)}(\omega, \mathbf{x}', e)}{\partial e} \right| \left| \frac{\partial \gamma^{(n)}(\omega, \mathbf{x}', r)}{\partial r} \right| \left| \frac{\partial(|\bar{\mathbf{k}}(\omega, r, e, \mathbf{x}')|)}{\partial \omega} \right| \times \\ & |\bar{\mathbf{k}}^{(n)}(\omega, r, \mathbf{x}'; e)| [\Upsilon_m^{(n)}(\omega, \mathbf{x}')]^{-1} g_{\dagger}^{(n)}(\omega, \mathbf{x}', e) g_{\dagger}^{(n)}(\omega, \mathbf{x}', r), \end{aligned} \quad (47)$$

where

$$g_{\dagger}^{(n)}(\omega, \mathbf{x}, \mathbf{x}') = [A^{(n)}(\omega, \mathbf{x}, \mathbf{x}')]^{-1} \exp \left(-i[\phi^{(n)}(\omega, \mathbf{x}, \mathbf{x}') + \pi/4] \right). \quad (48)$$

Here, g_{\dagger} is termed *reciprocal* Green's function, where \dagger indicates that the Green's function is reversed in both phase and amplitude. Note also that for $g_{\dagger}^{(n)}(\omega, \mathbf{x}', r)$, which acts on $\delta g_{res}(m^{(n)}; \omega, r, e)$, the reciprocity of Green's function has been used [42]. In addition, in Eq. (47), the parameters $|\partial\gamma(\omega, \mathbf{x}', e)/\partial e|\Delta e$ and $|\partial\gamma(\omega, \mathbf{x}', r)/\partial r|\Delta r$ are approximated using finite differences

$$\left| \frac{\partial\gamma(\omega, \mathbf{x}', e)}{\partial e} \right| \Delta e \approx \frac{1}{2} |\gamma(\omega, \mathbf{x}', e+1) - \gamma(\omega, \mathbf{x}', e-1)| \quad (49)$$

and

$$\left| \frac{\partial\gamma(\omega, \mathbf{x}', r)}{\partial r} \right| \Delta r \approx \frac{1}{2} |\gamma(\omega, \mathbf{x}', r+1) - \gamma(\omega, \mathbf{x}', r-1)|, \quad (50)$$

where the subscript $\gamma(\omega, \mathbf{x}', e \pm 1)$ (resp. $\gamma(\omega, \mathbf{x}', r \pm 1)$) denotes the adjacent emitters (resp. receivers).

The backprojection operator in Eq. (47) corrects for the decay in amplitude and shift in phase of the scattered waves via reversing the incident and scattering Green's functions. The factors $|\partial\gamma(\omega, \mathbf{x}', e)/\partial e|\Delta e$ and $|\partial\gamma(\omega, \mathbf{x}', r)/\partial r|\Delta r$ correct for the nonuniformity and sparsity of the angles the emitters and receivers are seen by any scattering point \mathbf{x}' in the medium, respectively. In addition, the Born approximation is naturally based on a low-frequency assumption, and assumes that the waves originated on emitter position e and measured on receiver position r can be affected by scattering on any points in the medium. Instead, the backprojection operator derived in Eq. (47) implies that the high-frequency waves dominate the scattered waves. The correction factors $|\bar{\mathbf{k}}| |\partial(|\bar{\mathbf{k}}|)/\partial\omega|$, which includes the scattering angles θ , enforces an assumption that for the waves originated on emitter position e , the scatterers in some vicinity of a ray linking the emitter-receiver positions (e, r) will affect the scattered waves on receiver position r more likely than scatterers far way from this linked ray. This high-frequency assumption agrees with the assumption of smoothness of the wavenumber map $k^{(n)}$ that was used for the two approximations (32) and (33), because this smoothness assumption is more accurate at high frequencies.

Finally, the squared slowness is updated using $m^{(n+1)} = m^{(n)} + \tau \delta m^{(n)}$, where τ is the step length, which is fixed for all n . The update $c^{(n+1)}$ can then be obtained from $m^{(n+1)}$.

4. RAY TRACING

This section describes a numerical implementation of the method described above for implementing UST. Specifically, this section explains how the ray theory based on a high frequency approximation and satisfying the *Eikonal* equation (10) and *Transport* equation (11) is used for computing the terms in the approximate Green's function and its reciprocal variant for heterogeneous and absorbing media.

The Eikonal equation can be expressed in the form of a Hamiltonian [45]

$$H(\mathbf{x}, \mathbf{k}) = \frac{1}{2} k^{-1} [\mathbf{k} \cdot \mathbf{k} - k^2], \quad (51)$$

where we recall that k is the real part of $\tilde{\mathbf{k}}$, and is dependent on c through Eq. (3). The Hamiltonian yields $H = 0$ along a reference ray satisfying the canonical equations

$$\begin{aligned} \dot{\mathbf{x}} &= \nabla_{\mathbf{k}} H \\ \dot{\mathbf{k}} &= -\nabla_{\mathbf{x}} H. \end{aligned} \quad (52)$$

For each emitter-receiver pair (e, r) , a canonical vector of the reference ray is introduced as $\mathbf{y}(s) = [\mathbf{x}(s), \mathbf{k}(s)]^T$, where s is the arc length on the ray, and T is the transpose operator. Here, the initial position \mathbf{x}_0 of the reference ray matches the emitter position e , and has an arc length s_0 , i.e., $\mathbf{x}_0 = \mathbf{x}(s_0) = e$, and the initial wavevector $\mathbf{k}(s_0)$ is chosen such that the reference ray is intercepted by the receiver position r after travelling through the medium. This is done through ray linking [34], which will be explained at the end of this section. Further details about how the rays are sampled in terms of the arc length, s , are given in the next section.

The contributions of the amplitude factor A in Eq. (9) from the geometrical spreading is A_{geom} , and is determined by *Transport* equation (11), which describes how the area of the ray tube changes compared to a reference point on the ray, and relies on the concept of the ray Jacobian [29]. In [3], the ray Jacobian was defined by the rate at which two closely-spaced rays diverge, and was computed for each linked ray using finite differences. (cf. [29], section 3.10.4.3.) Computing the ray Jacobian using finite differences requires at least two additional auxiliary rays for each linked ray (or emitter-receiver pair) in 2D. Here, the ray Jacobian is computed using *paraxial* ray tracing, also known as *dynamic* ray tracing. Instead of tracing auxiliary rays independent of the reference ray, paraxial ray tracing involves solving an additional system of linear ordinary differential equations for tracing paraxial ray, which can be solved along with the ray tracing system for the reference ray. (cf. [29], section 3.10.4.4.) Here, for each pair of emitter-receiver positions, a paraxial ray is traced along a reference ray which has been already computed through ray linking, i.e., a reference ray which links the corresponding emitter-receiver pair.

Accordingly, a paraxial ray is defined by the first-order approximation $\mathbf{y}(s) + \delta\mathbf{y}(s)$, where $\delta\mathbf{y}(s) = [\delta\mathbf{x}(s), \delta\mathbf{k}(s)]^T$ is the perturbation to the canonical vector of the reference ray, and satisfies the paraxial ray tracing system of equations

$$\delta\dot{\mathbf{y}} = \mathbf{D} \delta\mathbf{y}, \quad (53)$$

where

$$\mathbf{D} = \begin{bmatrix} \nabla_{\mathbf{x}} \nabla_{\mathbf{k}} H & \nabla_{\mathbf{k}} \nabla_{\mathbf{x}} H \\ -\nabla_{\mathbf{x}} \nabla_{\mathbf{x}} H & -\nabla_{\mathbf{k}} \nabla_{\mathbf{x}} H \end{bmatrix}. \quad (54)$$

Using the ray equations (52), the ray's position \mathbf{x} and wavevector \mathbf{k} satisfy the ray equations

$$\dot{\mathbf{x}} = k^{-1}\mathbf{k}, \quad \dot{\mathbf{k}} = \frac{1}{2}\nabla k[k^{-2}\mathbf{k} \cdot \mathbf{k} + 1], \quad (55)$$

where we remind that $k^{-2}|\mathbf{k}|^2 = 1$ for $H = 0$.

Also, using (53) and (54), the paraxial ray equations yield

$$\begin{aligned} \delta\dot{\mathbf{x}} &= \left[\frac{\partial}{\partial \mathbf{x}} \dot{\mathbf{x}} \right] \delta\mathbf{x} + \left[\frac{\partial}{\partial \mathbf{k}} \dot{\mathbf{x}} \right] \delta\mathbf{k} \\ \delta\dot{\mathbf{k}} &= \left[\frac{\partial}{\partial \mathbf{x}} \dot{\mathbf{k}} \right] \delta\mathbf{x} + \left[\frac{\partial}{\partial \mathbf{k}} \dot{\mathbf{k}} \right] \delta\mathbf{k}, \end{aligned} \quad (56)$$

where

$$\frac{\partial}{\partial \mathbf{x}} \dot{\mathbf{x}} = -k^{-2}\mathbf{k}\nabla k^T, \quad \frac{\partial}{\partial \mathbf{k}} \dot{\mathbf{x}} = k^{-1}, \quad \frac{\partial}{\partial \mathbf{x}} \dot{\mathbf{k}} = \nabla^2 k - k^{-1}\nabla k\nabla k^T, \quad \frac{\partial}{\partial \mathbf{k}} \dot{\mathbf{k}} = k^{-2}\nabla k\mathbf{k}^T. \quad (57)$$

Here, the paraxial ray tracing system defined by (55) and (56) is numerically implemented using a second-order variant of Runge-Kutta (RK) scheme, known as Heun's method, which provides a good compromise between accuracy and speed [43, 44]. An outline of the Heun's approach for solving the paraxial ray tracing system is given in Algorithm 1. In this algorithm, the normalisation steps applied on the wavevector \mathbf{k} act as a safeguard for improving stability of the algorithm in

presence of wavenumber maps with sharp gradients in an open-source toolbox [1]. Our numerical results show that for ray tracing in soft tissues like the breast with refractive index changes between $0.9 - 1.1$, these normalisation steps do not affect rays' trajectories and can be ignored.

The system (53) is a ray, if the perturbation vector $\delta\mathbf{y}$ satisfies

$$\delta H = \nabla_{\mathbf{k}} H \cdot \delta\mathbf{k} + \nabla_{\mathbf{x}} H \cdot \delta\mathbf{x} = 0. \quad (58)$$

In addition, considering (55), δH is constant along any solutions of the paraxial system, so it is sufficient to ensure the condition (58) on the initial point [45].

Initial conditions: The initial wavevector is specified by the frequency ω , the sound speed in water c_0 and the initial unit vector. Following [3], the rays are initialised on emitter e and are connected to receiver position r through ray linking [34]. Ray-linking is in class of shooting methods, and seeks to find a ray's trajectory which provides the stationary path within a family of neighborhood paths between e and r by enforcing a boundary condition on the ray's path such that the ray initialised on emitter position e is intercepted by the receiver position r after travelling across the medium. For each iteration (linear subproblem) of the UST inverse problem, and emitter–receiver pair (e, r) , ray linking is performed by iteratively determining the initial unit direction of the ray initialised on e using an optimisation algorithm such that the interception point of the ray by the detection surface (ring) matches the receiver position r within a tolerance [29, 46]. Having determined the initial wavevector $\mathbf{k}(s_0)$ and using the condition (58), together with enforcing the constraint $\delta\mathbf{x}(s_0) = 0$, the initial perturbation to the wavevector, $\delta\mathbf{k}(s_0)$, must satisfy $\mathbf{k}(s_0) \cdot \delta\mathbf{k}(s_0) = 0$.

Grid-to-ray interpolation: The squared slowness map is updated on the grid points, so for implementing algorithm 1, it must be interpolated onto the rays' sampled points. Here, the grid-to-ray interpolation was performed using a B-spline interpolation, which provides continuous values for ∇k and $\nabla^2 k$ at any arbitrary (offgrid) point. (For further details, see [3].)

Ray-to-grid interpolation: The parameters of the Green's function on the grid points are computed by interpolation from the linked rays onto the grid points using a trilinear interpolation [3].

5. RAY COORDINATES

This section describes how the Green's function included in the residual (19) and its reciprocal variants included in the backprojection operator (47) are approximated and discretised along the linked rays. (See Eq. (46).) The formulae will be derived for $g(\omega, r, e)$ and $g_{\dagger}(\omega, \mathbf{x}, e)$, but the formulae derived for the latter can also be applied on $g_{\dagger}(\omega, \mathbf{x}, r)$ after interchanging e and r . In general, for the 2D case, rays are defined using two coordinates: one specifying the initial direction (angle) of the ray and another a monotonic parameter along the ray [29]. Here, the ray parameters are chosen the initial angle, θ , and the arc length, s .

Definition 1. The trajectory of a ray linking an emission point e to a reception point r is defined by the sampled arc lengths s_i , $i \in \{0, \dots, M_{(e,r)}\}$. Therefore, the sampled points are initialised at s_0 with $\mathbf{x}(s_0) := e$, and are terminated at $s_{M_{(e,r)}}$ with $\mathbf{x}(s_{M_{(e,r)}}) := r$, the position of receiver r . The sampled arc length s_i satisfy

$$s_i = \begin{cases} i\Delta s, & i \in \{0, \dots, M_{(e,r)} - 1\} \\ (i-1)\Delta s + \Delta s', & i = M_{(e,r)}. \end{cases} \quad (59)$$

Here, the second line is used in order to indicate that the last point of the ray must be matched to the reception point r , and therefore $\Delta s' = s_{M_{(e,r)}} - s_{M_{(e,r)}-1}$ with $\Delta s' \leq \Delta s$ [34].

Algorithm 1 Paraxial ray tracing for the linked ray initialised on e and intercepeted by r using Heun's method

```

1: input:  $(e, r)$ ,  $k := k(\mathbf{x})$             $\triangleright$  Input emitter and receiver positions and wavenumber map
2: initialise:  $\mathbf{x} = e, \mathbf{k}$        $\triangleright$  Set initial position, and compute the initial wavevector through ray linking
3:  $\delta\mathbf{x} = 0, \delta\mathbf{k}$  satisfying  $\delta\mathbf{k} \cdot \mathbf{k} = 0$ ,            $\triangleright$  Set initial conditions: paraxial ray (amplitude)
4: while  $\mathbf{x}(s)$  is inside  $\Omega$  do
5:
6:   — — —
7:    $\mathbf{k} \leftarrow k \mathbf{k} / |\mathbf{k}|$             $\triangleright$  Update reference ray
8:    $q_x = \mathbf{k}/k$             $\triangleright$  Normalise the ray direction
9:    $q_k = \nabla k(\mathbf{x})$             $\triangleright$  Compute the update variables
10:   $\mathbf{k}' \leftarrow \mathbf{k} + \Delta s q_k$             $\triangleright$  Update the auxiliary ray direction
11:   $k' \leftarrow k(\mathbf{x} + \Delta s q_x)$             $\triangleright$  Update the auxiliary wavenumber
12:   $\mathbf{k}' \leftarrow k' \mathbf{k}' / |\mathbf{k}'|$             $\triangleright$  Normalise the auxiliary ray direction
13:   $q'_x = \mathbf{k}' / k'$             $\triangleright$  Compute the auxiliary update variables
14:   $q'_k = \nabla k(\mathbf{x} + \Delta s q_x)$ 
15:   $\mathbf{x} \leftarrow \mathbf{x} + \Delta s [q_x + q'_x] / |q_x + q'_x|$             $\triangleright$  Update the ray position
16:   $\mathbf{k} \leftarrow \mathbf{k} + \Delta s [q_k + q'_k] / 2$             $\triangleright$  Update the ray direction
17:
18:  — — —            $\triangleright$  Update paraxial ray: geometrical amplitude
19:   $q_{\delta\mathbf{x}} = [-\mathbf{k}\nabla k^T/k^2]\delta\mathbf{x} + [1/k]\delta\mathbf{k}$             $\triangleright$  Compute the update variables
20:   $q_{\delta\mathbf{k}} = [\nabla^2 k - \nabla k \nabla k^T/k]\delta\mathbf{x} + [\nabla k \mathbf{k}^T/k^2]\delta\mathbf{k}$ 
21:   $\delta\mathbf{k}' \leftarrow \delta\mathbf{k} + \Delta s q_{\delta\mathbf{k}}$             $\triangleright$  Update the auxiliary ray direction perturbation
22:   $\delta\mathbf{x}' \leftarrow \delta\mathbf{x} + \Delta s q_{\delta\mathbf{x}}$             $\triangleright$  Update the auxiliary ray position perturbation
23:   $q'_{\delta\mathbf{x}} = [-\mathbf{k}'\nabla k'^T/k'^2]\delta\mathbf{x}' + [1/k']\delta\mathbf{k}'$             $\triangleright$  Compute the auxiliary update variables
24:   $q'_{\delta\mathbf{k}} = [\nabla^2 k' - \nabla k' \nabla k'^T/k']\delta\mathbf{x}' + [\nabla k' \mathbf{k}'^T/k'^2]\delta\mathbf{k}'$ 
25:   $\delta\mathbf{x} \leftarrow \delta\mathbf{x} + \Delta s [q_{\delta\mathbf{x}} + q'_{\delta\mathbf{x}}] / 2$             $\triangleright$  Update the ray position perturbation
26:   $\delta\mathbf{k} \leftarrow \delta\mathbf{k} + \Delta s [q_{\delta\mathbf{k}} + q'_{\delta\mathbf{k}}] / 2$             $\triangleright$  Update the ray direction perturbation
27:
28: end while

```

Definition 2. For each emitter position e , the parameters of the Green's function initialised on e are approximated on a set of linked rays $f_{(k,r,e)} = 0$. These rays are parameterised in space as $\mathbf{x}(s_i, \theta_{(r,e)})$, which denotes the position on the arc length s of the sampled point i along a ray linking the emission position e to the reception position r . Also, the polar initial direction of this ray is indicated by $\theta_{(r,e)}$.

Accordingly, the Green's function $g(\omega, \mathbf{x}, e)$ and its reciprocal variant $g_\dagger(\omega, \mathbf{x}, e)$ are discretised on the points sampled on the rays linking emitter position e to all receiver positions r using the coordinates defined in Definition 2 in the form

$$g_\dagger(\omega, \mathbf{x}(s_i, \theta_{(r,e)}), e) \approx A(\omega, \mathbf{x}(s_i, \theta_{(r,e)}), e) \exp\left(i[\phi(\omega, \mathbf{x}(s_i, \theta_{(r,e)}), e) + \pi/4]\right) \quad (60)$$

and

$$g_\dagger(\omega, \mathbf{x}(s_i, \theta_{(r,e)}), e) \approx [A(\omega, \mathbf{x}(s_i, \theta_{(r,e)}), e)]^{-1} \exp\left(-i[\phi(\omega, \mathbf{x}(s_i, \theta_{(r,e)}), e) + \pi/4]\right), \quad (61)$$

where $e := \mathbf{x}(s_0, \theta_{(r,e)})$ for all r . (cf. Eq. (9) and (48).) In (60) and (61), the accumulated phase ϕ is discretised in the form

$$\phi(\omega, \mathbf{x}(s_i, \theta_{(r,e)}), e) = \int_{s_0}^{s_i} k(\mathbf{x}(s_i, \theta_{(r,e)})) \, ds - \frac{\pi}{2} \mathcal{K}(s_i, \theta(r, e)), \quad (62)$$

where $\mathcal{K}(s_i, \theta(r, e))$ is the cumulative times the sign of the ray Jacobian along the ray has been changed. Points on which the ray Jacobian changes sign are called *caustics*, and will lead to a $\pi/2$ shift in the phase [29].

The contributions of the amplitude factor A from absorption, A_{abs} , is discretised in the form

$$A_{abs}(\omega, \mathbf{x}(s_i, \theta_{(r,e)}), e) = \exp \left(- \int_{s_0}^{s_i} \alpha(\mathbf{x}(s_i, \theta_{(r,e)})) \, ds \right). \quad (63)$$

The contributions of the amplitude factor A from the geometrical spreading, A_{geom} , is determined by the relative change of the ray Jacobian along the ray with respect to a reference point on which the amplitude can be determined analytically [47]. Correspondingly, the Jacobian J on the point i along the ray initialised by angle $\theta_{(r,e)}$ satisfies

$$J(s_i, \theta_{(r,e)}) = \det \Xi(s_i, \theta_{(r,e)}), \quad (64)$$

where Ξ is the *transformation matrix* from the ray coordinates $\gamma = [\gamma_1, \gamma_2]^T$ to the general Cartesian coordinates $\mathbf{x} = [\mathbf{x}_1, \mathbf{x}_2]^T$, and is in the form $\Xi = \partial \mathbf{x} / \partial \gamma$.

In general, γ_1 must be a parameter specifying the ray, and γ_2 must be a monotonic parameter along the ray. (See [29], section 3.10.) Here, $\gamma_1 = \theta$ and $\gamma_2 = s$, as discussed in Definition 2. The geometrical attenuation A_{geom} now satisfies

$$A_{geom}(\omega, \mathbf{x}(s_i, \theta_{(r,e)}), e) = \left[\frac{c(\mathbf{x}(s_i, \theta_{(r,e)}))}{c(\mathbf{x}(s_1, \theta_{(r,e)}))} \frac{J(s_1, \theta_{(r,e)})}{J(s_i, \theta_{(r,e)})} \right]^{1/2} A_{geom}(\omega, \mathbf{x}(s_1, \theta_{(r,e)}), e), \quad (65)$$

where s_1 is the arc length of the first sampled point after the initial point on the ray, and is chosen as the reference point, using an assumption that a neighborhood of the emitter positions with a radius greater than ray spacing Δs is acoustically homogeneous, and therefore, $A_{geom}(\omega, \mathbf{x}(s_1, \theta_{(r,e)}), e)$ can be calculated analytically using the geometrical attenuation formula (16) and by setting $\mathbf{x}_{ref} := \mathbf{x}(s_1, \cdot)$ [29].

6. NUMERICAL RESULTS

This section describes numerical experiments demonstrating the effectiveness of the proposed ray-based inversion approach for a low-cost computation of a high-resolution image of the sound speed distribution inside the breast.

6.1. Data simulation. An imaging system consisting of 64 emitters and 256 receivers uniformly distributed along a circular ring with radius $R = 9.5\text{cm}$ was simulated. A horizontal slice of a 3D digital phantom, which mimics the acoustic properties of the breast and is freely available [48], was used in this study. The sound speed was set to a range $1470\text{--}1580\text{ ms}^{-1}$, and the absorption coefficient α_0 was set to a range $0\text{--}1\text{ dBMHz}^{-y}\text{cm}^{-1}$, and the power law exponent y was set to 1.4. Figures 1(a) and 1(b) show the maps for the sound speed and absorption coefficient of the breast phantom, respectively. The sound speed and absorption coefficient in water was set 1500 ms^{-1} and 0, respectively. The computational grid consisted of 502×502 grid points with position $[-10.04, +10.00] \times [-10.04, +10.00]\text{cm}^2$ and a grid spacing of $\Delta x = 4 \times 10^{-2}\text{cm}$ along all the Cartesian coordinates. Using this sound speed distribution and grid spacing, the maximum frequency supported by the grid, f_{\max} , was 1.84 MHz.

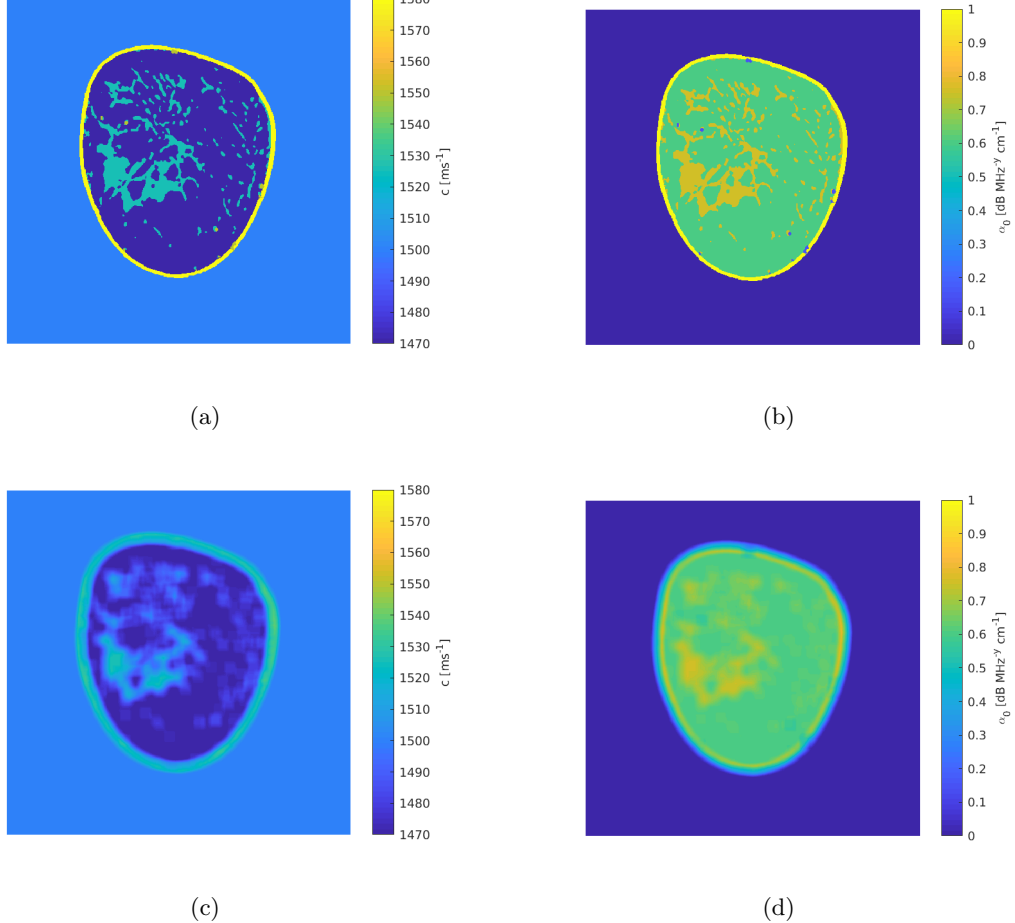


FIGURE 1. Phantom used for simulation of the synthetic UST data using the full-wave approach: (a) sound speed [ms^{-1}], (b) absorption coefficient [$\text{dB MHz}^{-1} \text{cm}^{-1}$], (c) smoothed sound speed [ms^{-1}], (d) smoothed absorption coefficient [$\text{dB MHz}^{-1} \text{cm}^{-1}$]. The maps are shown on a grid consisting of 502×502 points (used for the wave simulation). The maps (c) and (d) are smoothed by applying an averaging window of size 17 points on the original acoustic maps (a) and (b), respectively. The original (nonsmoothed) acoustic maps were used for simulating the data used for image reconstruction, and the smoothed maps were used for simulating the data used as a benchmark for comparison with the ray approximation to heterogenous Green's function. The power law exponent was assumed $y = 1.4$ and homogeneous.

Simulating time series data. A k -space *pseudo-spectral* method was used to simulate the acoustic pressure time series data on the detection ring after being produced by each time-varying source. This numerical approach was used to solve a system of three-coupled first-order wave equations, equivalent to the Szabo's second-order wave equation. The Szabo's wave equation is a time-domain variant of Eq. (2) with the complex wavenumber defined by (3) [35, 36, 37, 38]. The emitters and receivers were assumed as points placed on the circle, and the interpolation of the pressure field

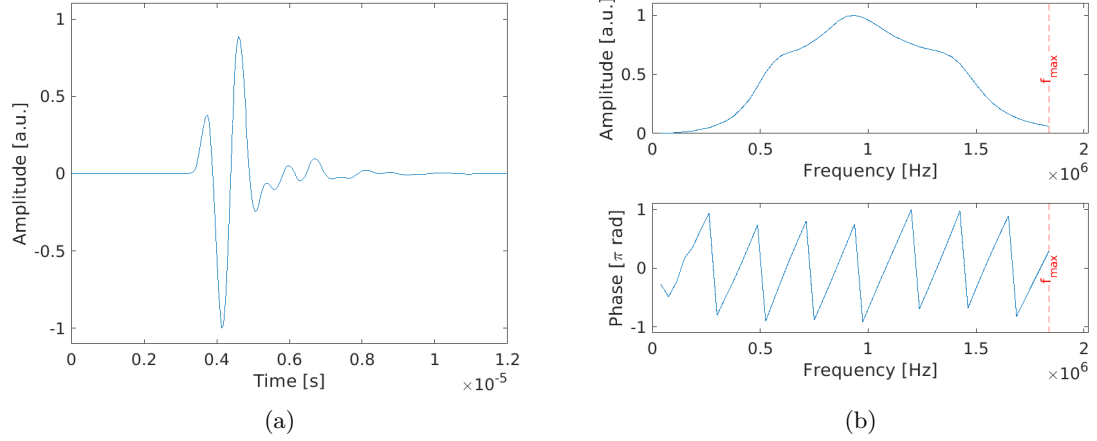


FIGURE 2. Acoustic source used for all excitations (emitters): (a) time domain, (b) frequency domain: normalised amplitude and phase. f_{max} indicates the maximum frequency supported by the grid used for the wave simulations.

between the grid and these transducers was performed using a Fourier approach [38]. To simulate the data, each emitter was individually driven by an excitation pulse, and the induced acoustic pressure time series were recorded on the receivers at 6466 time points with a sampling rate of 39.6MHz (25.25 ns time spacing). This was repeated for each emitter. Figure 2(a) shows the normalised amplitude of the acoustic source in the time domain, and figure 2(b) shows the normalised amplitude and phase components of the acoustic source in frequency domain, respectively. This signal is used as the acoustic source for all excitations.

6.2. Numerical validation of the ray approximation to the Green's function. In this section, the approximate Green's function solution to Szabo's wave equation is compared to a full-wave solution using the k-space pseudo-spectral method [36, 37, 38] in a heterogeneous and absorbing medium with a spatially smooth variations in acoustic properties. It must be reminded that the approximate heterogeneous Green's function was introduced in section 2, and its numerical approximation and discretisation were explained in sections 4 and 5, respectively. Further details about derivation of the Green's function solution to Szabo's wave equation were given in [3]. For the full-wave approach, emitter 1 was excited by the acoustic pulse shown in figures 2(a), and the induced pressure propagated across the breast in water, and was recorded on all the 256 receivers. The Green's function $g(\omega, r, e)$ depends only on the accumulated parameters and geometrical spreading along the linked rays, and does not incorporate the scattering effects. Therefore, for a fair comparison with the full-wave simulation, the scattering effects were minimised in the full-wave simulation by applying an averaging window of size 17 grid points on the sound speed and absorption coefficient maps. The smoothed sound speed and absorption coefficient maps are shown in figures 1(c) and 1(d), respectively.

For the ray-approximation approach, the Green's function was approximated along the linked rays, and was then included in the Green's formula (5) in order to approximate the pressure time series on the receivers after an excitation of emitter 1. Note that in (5), the integral in space is dropped for a point source. In the image reconstruction below, the inverse crime was avoided by using two different computational grids for data simulation and image reconstruction. (Note that using

different grids may not be necessary in our study, because two inherently different approaches are used for the data simulation and image reconstruction.) For ray-based image reconstruction below, the computational grid has a size 204×204 points with a grid spacing of 1 mm. Therefore, the ray approximation to the Green's function used for comparison with the full-wave simulation was also performed on the same grid. For implementing the ray approximation to the Green's function, the smoothed sound speed and absorption coefficient maps used for the full-wave simulation were interpolated onto the grid for image reconstruction, and the interpolated wavenumber map was smoothed again by an averaging window of size 7 points in order to minimise interpolation effects. (Compared to the grid for full-wave simulation, the averaging window size was reduced reciprocally to the increase in the grid spacing.) The pressure field produced by emitter 1 was approximated on all the 256 receivers at a single frequency 1 MHz and for three cases: only water, non-absorbing breast and absorbing breast inside water.

Figure 3(a) shows the phase of the pressure time series on all the receivers after an excitation of emitter 1. (The phases were wrapped to $[-\pi, \pi]$.) The green plot shows the phases which are analytically computed using the homogeneous Green's function by assuming only water, and the red plot shows the phases computed using the ray approximation to the Green's function for the absorbing breast inside water. Also, the phase of the pressure time series simulated by the full-wave approach for the absorbing breast inside water was shown by the blue plot. As shown in this figure, for receivers in the range 50-180, for which the linked rays travel through the breast (not only water), the ray approximation to the heterogeneous and absorbing Green's function and the full-wave simulation have very good agreement, but the Green's function analytically calculated by assuming only water has large discrepancies with the full-wave simulation.

Figure 3(b) shows the amplitude of the pressure time series on all the receivers after an excitation of emitter 1. The green plot shows the amplitudes computed by the analytic Green's function assuming only water. The amplitudes computed using the Green's function assuming a nonabsorbing breast, i.e., the amplitudes attenuated by only the geometrical spreading, were approximated on all the receivers using Eq. (65), and are shown by the light blue plot. It must be reminded that for computing Eq. (65), the rays' Jacobian was approximated using paraxial ray tracing, as discussed in section 4. The amplitudes computed using the Green's function for the absorbing breast were approximated as the product of the amplitude decay because of geometrical spreading (the light blue plot) and the accumulated acoustic absorption, and are shown by the red plot. The accumulated acoustic absorption was computed using Eq. (63). The amplitudes of the pressure time series simulated by the full-wave approach and recorded on all the receivers are shown by the dark blue plot. As shown in this figure, for the absorbing breast, the amplitudes computed by the product of the geometrical spreading using paraxial ray tracing and the accumulated acoustic absorption have very good agreement with the amplitudes computed using the full-wave simulation, but the analytically calculated Green's function assuming only water or the heterogeneous Green's function neglecting the acoustic absorption have large discrepancies with the full-wave simulation.

6.3. Image reconstruction. This section explains the procedure for a ray-based image reconstruction from ultrasound data simulated using the full-waveform approach, and shows the reconstructed images. Accordingly, a k-space pseudo-spectral approach was used for simulating two sets of synthetic data for a time-varying and point source, as described in section 6.1. The first data set was simulated for only water, and the second data set was simulated for the digital breast phantom inside water. The breast-in-water data was simulated using the sound speed and absorption coefficient maps shown in figures 1(a) and 1(b), respectively. For simulating each data set, each emitter was excited by the excitation pulse shown in figure 2(a), and the simulated pressure time series

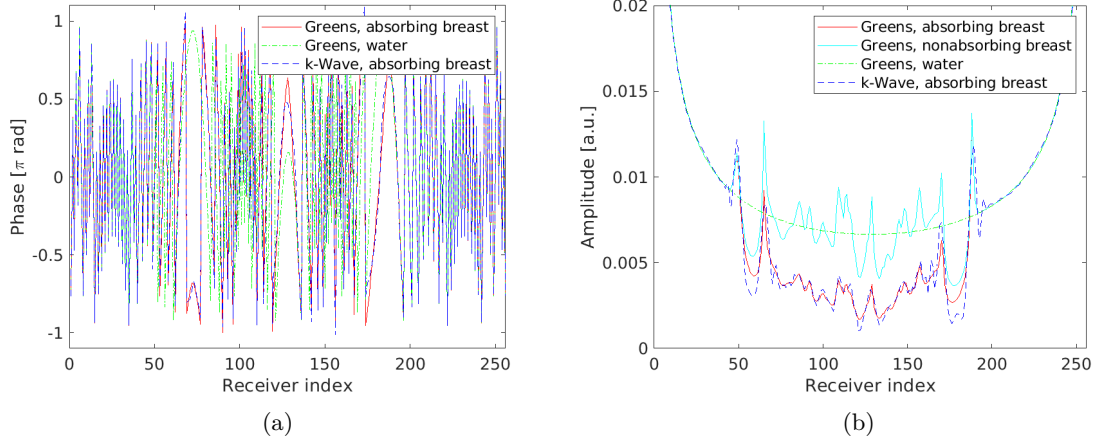


FIGURE 3. The pressure time series on all the receivers at single frequency 1 MHz after an excitation of emitter 1: (a) phase, (b) amplitude.

were recorded on all the receivers in time. The excitation and measurements were sequentially repeated for all the emitters. The computational time for simulation of the UST data set including all the excitations for the digital breast phantom inside water using the k-Wave's Matlab code [38] on a single 8-core Xeon E5-2620 v4 2.1 GHz CPU was about 5 hours. Different levels of additive white Gaussian noise (AWGN) were added to the simulated pressure time series to provide 40 dB, 30 dB and 25 dB signal-to-noise ratio (SNR) of the peak amplitudes for both breast-in-water and only-water data sets.

For reducing an inverse crime in time spacing, the time series simulated by the full-waveform approach on the receivers were temporally downsampled by factor 2 before ray-based image reconstruction. Also, the grid for image reconstruction consisted of 204×204 grid points with position $[-10.1650, +10.1350] \times [-10.1650, +10.1350] \text{cm}^2$ and a grid spacing of $\Delta x = 1 \text{mm}$ along all the Cartesian coordinates. The image reconstruction was performed on the grid points inside a binary mask with radius 0.95 of the radius of the detection ring, and the sound speed on the grid points outside this binary mask was set to the sound speed of water, 1500 ms^{-1} . The Green's function g , which is included in the residual δg_{res} , is directly approximated on the receivers through ray linking. However, because the sound speed is reconstructed on the grid points, the parameters of the reciprocal Green's functions g_{\dagger} , which are approximated on the linked rays, must be interpolated onto the grid points. The interpolations of approximated parameters of the reciprocal Green's function from linked rays onto grid points were done by enforcing a triangulation on the sampled points on the linked rays and using a trilinear interpolation. In addition, the reciprocal Green's functions $g_{\dagger}(\omega, \mathbf{x}, r)$ were computed without additional ray tracing and by only reversing the accumulated parameters on the linked rays associated with the Green's functions $g(\omega, r, e)$ [3]. Note that for approximating the geometrical portion of the amplitudes for $g(\omega, \mathbf{x}, r)$, an additional paraxial ray must be traced along each reversed ray. The Green's function $g_{\dagger}(\omega, \mathbf{x}, r)$ can then be obtained from $g(\omega, \mathbf{x}, r)$ by computing the reciprocal to phases and amplitudes.

6.3.1. Inversion approach using time-of-flights (initial guess). Because the objective function in Eq. (18) is highly nonlinear, an initial guess is often used [12, 13]. Here, an image reconstruction approach based on direct time of flights (TOFs) of the measured (simulated) pressure time series

was used to provide an initial guess. The TOF-based inversion approach iteratively minimises the L2 norm of discrepancy between the TOFs modelled by the ray tracing algorithm and the TOFs obtained from the measured (simulated) pressure time series using a first-arrival picking algorithm [11]. The effects of measurement errors on the picked first-arrivals were compensated for using a difference inversion approach, in which the difference of the slowness $1/c$ for the breast in water and only water is computed from the discrepancy of the first-arrival times picked from the measured breast-in-water and only-water data sets. The minimisation is performed by iteratively linearising the associated objective function, and solving the arising linearised subproblems using a Radon-type technique. Here, each linearised subproblem was solved using a Simultaneous Algebraic Reconstruction Technique (SART) algorithm, which accounts for nonuniform ray density across the image due to the curved nature of rays [50]. For computing rays' trajectories at each linearisation, the sound speed update was smoothed by an averaging window of size 7 grid points, but integration of accumulated time-of-flights along trajectory of the linked rays was performed on the nonsmooth updates, i.e., the system matrix was constructed on the smoothed update of the sound speed, but the constructed system matrix was multiplied by the nonsmoothed sound speed update. The ray linking was performed using the Secant method such that for each emitter-receiver pair, the linked ray (the optimal ray after ray linking) for each linearisation is used as initial guess for ray linking for the next linearisation [34, 3]. The TOF-based algorithm was terminated after few linearisations to provide a good trade-off between accuracy and artefact due to the errors in the picked first-arrival times [3].

6.3.2. Inversion approaches using ray approximation to heterogeneous Green's function. Below, the procedure for implementing the inversion approach based on the Green's function is explained. For evaluating the effectiveness of the proposed Hessian-free inversion approach, the approach used in [3] was used as the benchmark. The image reconstruction is determining the squared slowness map, m , which minimises the objective function (18). The inverse problem is solved via discretising the objective function at a number of frequencies within the frequency range of the transducers, and linearisation and minimisation of the objective function from low to high frequencies until the computed update direction for the linearised subproblem associated with a frequency set becomes smaller than a tolerance. For computing the residual (19), the measured Green's function $\hat{g}(\omega, r, e)$ is derived by deconvolving the excitation pulse from the measured (simulated) pressure time series. Here, the deconvolution was performed using a Tikhonov regularised inversion approach in the frequency domain [49]. Also, each Green's function $g(m; \omega, r, e)$ included in the residual (19) is approximated on the last points of the linked rays computed on the last update of the sound speed. *Ray linking.* For the TOF-based and the Green's function-based approaches, the ray linking was performed on the updates of the sound speed and wavenumber maps for each of emitter-receiver pairs separately. For each update of the wavenumber map and each emitter-receiver pair, the ray linking was done by iteratively updating the initial unit direction of the ray using a Secant method [3, 34, 46]. The initial guess for the unknown initial unit direction of the ray was set the obtained optimal initial direction after ray linking for the last previous update of the wavenumber map, and the ray's trajectory was iteratively computed using the first part of Algorithm 1 until the interception point of the ray by the detection ring matches the receiver position within a tolerance. The parameters of Green's functions g and reciprocal Green's functions g_\dagger (included in the backprojection formula for the Hessian-free approach) were computed along the linked rays. (See the formulae given in section 5.) For computing the geometrical portion of amplitudes, linked rays are used as reference rays, and paraxial rays are computed in vicinity of the reference rays via implementing the second part of Algorithm 1. For ray tracing and ray linking, an averaging window

of size 7 grid points was applied on the updated wavenumber maps, but integration along the linked rays and approximating the Green's functions using the formulae in section 5 were applied on the nonsmoothed updates.

a) Hessian-free ray-born inversion. The inversion approach described in section 3 was implemented at 140 discretised frequencies in the range $f \in \{0.2, \dots, 1.5\}$ MHz. The image reconstruction was performed from low to high frequencies such that each update of the squared slowness map was computed at two consecutive discretised frequencies using Eq. 46. ($n \in \{1, \dots, 70\}$.) For each linearisation n , the Green's functions $g(\omega, r, e)$, which are included in the residual (19), and the reciprocal Green's functions $g_{\dagger}(\omega, \mathbf{x}, e)$ and $g_{\dagger}(\omega, \mathbf{x}, r)$, which are included in the backprojection formula (47), were computed on the forward and backward rays, the rays which are initialised on emitter positions e and receiver positions r , respectively. The step length was heuristically chosen $\tau = 1.2 \times 10^{-1}$ for all linearisations. The major portion of the computational cost for solving each linear problem (24) is ray tracing, because the update direction is obtained in one step using (46). Therefore, using this inversion approach, the computational cost for solving each linearised subproblem is almost the same as each linearised subproblem in the TOF-based algorithm. Note that the total number of linearisations required for reaching an optimal point using this approach was almost five to ten times more than the TOF-based algorithm.

b) Hessian-based ray-born inversion (Gauss-Newton). Using $\mathcal{Q} = 1$ for all $(\omega, r, e, \mathbf{x})$, each arising linearised subproblem n (24) is solved via first forming the gradient $\nabla \mathcal{F}^{(n)}$ and then computing the update direction via iteratively computing the actions of the Hessian matrix $H^{(n)}$ on the updates of perturbation to the squared slowness map. This is equivalent to computing a Gauss-Newton search direction using inner iterations. The reader is referred to [3] for further details. Here, each linearised subproblem was solved using 10-15 inner iterations. Note that early stopping the inner iterations has regularising effects on the solution. In order to provide a benchmark for evaluating performance of the proposed Hessian-free ray-born inversion algorithm, the Gauss-Newton inversion approach described in [3] was implemented at 100 discretised frequencies in the range $f \in \{0.2, \dots, 1.1\}$ MHz. Like the Hessian-free approach, the image reconstruction was performed from low to high frequencies such that each update of the sound speed was computed at two consecutive discretised frequencies. ($n \in \{1, \dots, 50\}$.) Compared to the Hessian-free approach, the algorithm was terminated at smaller n , because solving linearised subproblems at frequencies larger than 1.1 MHz provided very small search directions. Note that as described in section 4, the geometrical portion of the amplitude was computed via solving a paraxial system of equations, not auxiliary rays, as done in [3]. (cf. Algorithm 1.) The step length was heuristically chosen $\tau = 3 \times 10^4$ for all linearisations. Using my developed code in a Matlab environment and using the CPU mentioned in the first paragraph in section 6.3, the computational time for solving each linearised subproblem n and computing each Gauss-Newton search direction was almost an order of magnitude more than solving each linearised subproblem associated with the proposed Hessian-free approach. As a comparison with a full-waveform inversion, the total computational time for reconstructing a sound speed image using the Gauss-Newton algorithm was almost the same as the computational time for simulating the breast-in-water UST data using the k-Wave, i.e., solving a single forward problem using the full-waveform approach [38]. As described in section 3, the sound speed updates, c , are obtained from updates of the squared slowness map, m .

6.4. Reconstructed images. In this section, the sound speed images reconstructed using the proposed Hessian-free ray-born inversion approach are shown, and are compared to the images reconstructed using the Gauss-Newton inversion approach [3]. It must be reminded that the proposed Hessian-free approach was almost an order of magnitude faster than the Gauss-Newton inversion

approach. The reconstructed images are evaluated in terms of Relative Error (RE), i.e.,

$$RE_{\text{image}} = \frac{\|c_{\text{image}} - c_{\text{phantom}}\|_2}{\|c_{\text{water}} - c_{\text{phantom}}\|_2} \times 100, \quad (66)$$

where c_{phantom} is the sound speed map of the digital breast phantom which is interpolated onto the grid for image reconstruction, and c_{image} is the reconstructed sound speed image. These stack vectors were computed on the grid points inside the binary mask for image reconstruction. The speed of sound of the grid points outside the binary mask was to the sound speed in water, i.e., $c_{\text{water}} = 1500 \text{ ms}^{-1}$. (cf. section 6.3.)

6.4.1. Reconstructed images from UST data with high SNR. Below, the reconstructed sound speed images from the synthetic ultrasound data with a high signal-to-noise ratio (SNR) are shown, and are evaluated in terms of RE. Figure 4(a) shows the sound speed map of the digital breast phantom (ground truth). Figure 4(b) shows the image reconstructed from time-of-flights of the time-series simulated with 40 dB SNR. The time-of-flights were computed using a modified Akaike-Information-Criterion (AIC) approach [11].

As described in section 2, the proposed forward model based on the ray approximation to heterogeneous Green's function can account for the acoustic absorption and dispersion, but the absorption coefficient α_0 map and the exponent power y are not known in a practical setting. Here, the exponent power was assumed known and set $y = 1.4$, and the image reconstruction was performed using three assumptions: known α_0 map (figure 1(b)), zero α_0 , and a homogeneous α_0 which can be determined in a practical setting. $\alpha = \alpha_0 \omega^y$ can be determined from the mean logarithmic relative amplitudes of the measured time series for the only-water to the breast-in-water data sets. (Here, the homogeneous absorption coefficient was heuristically set to $0.5 \text{ dBMHz}^{-y} \text{cm}^{-1}$.)

Figures 4(c) and 4(d) show the reconstructed sound speed images from the 40 dB-SNR synthetic ultrasound data using an assumption that α_0 map is known and using the Gauss-Newton and the proposed Hessian-inversion-free ray-born inversion approaches, respectively. In the same way, figures 4(e) and 4(f) show the reconstructed images using an assumption that α_0 is zero everywhere, i.e., the acoustic absorption and dispersion are neglected. Also, figures 4(g) and 4(h) show the reconstructed images assuming the homogeneous absorption coefficient $\alpha_0 = 0.5 \text{ dBMHz}^{-y} \text{cm}^{-1}$ inside the breast. The RE of the reconstructed images are written in the caption of the figure.

As shown in these figures, for the high-SNR UST data used in this experiment, the images reconstructed using the Gauss-Newton inversion approach, which is based on an implicit and iterative inversion of the full Hessian matrix, are more accurate than those reconstructed using the Hessian-free approach in terms of RE. That makes sense, because for high-SNR data, the approximations made for diagonalising the Hessian matrix, Eqs. (32) and (33), have reduced the computational cost in exchange for a slight degradation in the reconstructed image, compared to the Gauss-Newton approach which uses the full Hessian matrix. Furthermore, using both inversion approaches, an assumption of zero α_0 has led to less accurate images and with more artefact, but assuming homogeneous α_0 for the breast has significantly improved the reconstructed images in terms of RE, compared to an assumption of zero α_0 . It must be reminded that the exponent power was assumed known for both cases.

6.4.2. Reconstructed images from UST data with medium and low SNR. Below, the reconstructed images from simulated ultrasound data with medium and low SNR and using an assumption of homogeneous $\alpha_0 = 0.5 \text{ dBMHz}^{-y} \text{cm}^{-1}$ are presented. This assumption should hold for imaging the breast. Accordingly, figures 5(a) and 5(b) show the TOF-based images reconstructed from the UST synthetic data with 30 dB and 25 dB SNR, respectively. Figures 5(c) and 5(d) show the images

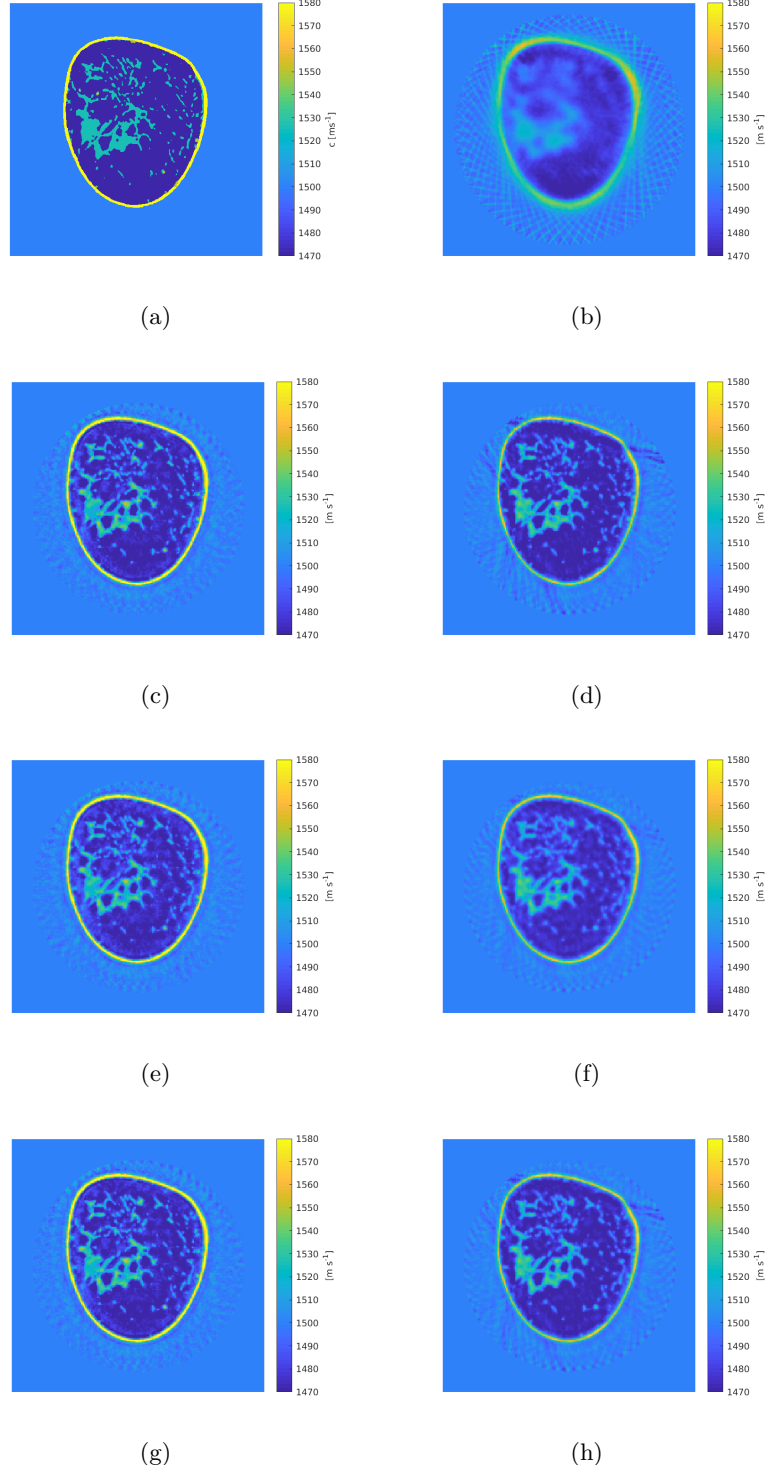


FIGURE 4. (a) Ground truth. Reconstructed sound speed images from UST data with 40dB SNR: (b) time-of-flight-based approach (initial guess), $RE = 73.42\%$. True α_0 (Figure 1(b)): (c) Gauss-Newton, $RE = 36.21\%$, (d) Hessian-free, $RE = 41.37\%$. $\alpha_0 = 0$: (e) Gauss-Newton, $RE = 39.98\%$, (f) Hessian-free, $RE = 44.58\%$. $\alpha_0 = 0.5 \text{ dB MHz}^{-1} \text{cm}^{-1}$ (homogeneous inside breast): (g) Gauss-Newton, $RE = 36.88\%$, (h) Hessian-free, $RE = 41.93\%$.

reconstructed using the Gauss-Newton inversion approach and from the UST data with 30 dB and 25 dB SNR, respectively. The equivalent figures 5(e) and 5(f) show images reconstructed using the proposed Hessian-free approach. As shown in figures 5(a)-5(d), an increase in the additive white Gaussian noise (a reduction in SNR) in the UST data has led to more artefact and greater RE in the TOF-based reconstructed images (initial guesses) and the images reconstructed using the Gauss-Newton inversion approach. Additionally, figures 5(e) and 5(f) show that for 30dB and 25dB SNR data, the images reconstructed using the proposed Hessian-free ray-born inversion approach have less artefact than the equivalent images reconstructed using the Gauss-Newton inversion approach. For the data with 25 dB SNR, the sound speed image reconstructed using the Hessian-free approach is more accurate than the Gauss-Newton approach in terms of RE.

Figures 6(a), 6(b) and 6(c) show the obtained sound speed values on the main diagonal of the grid for image reconstruction from UST data with 40 dB, 30 dB and 25 dB SNR, respectively. The equivalent sound speed values for the digital breast phantom, which was interpolated from the grid for the k-Wave simulation onto the grid for image reconstruction, are shown by the black colour. The sound speed values obtained using the TOF-based approach are shown by the green colour, and the values reconstructed using the Gauss-Newton and the proposed Hessian-free approaches are shown by the blue and red colours, respectively. As shown in these figures, the Hessian-free approach has reconstructed sharp sound speed changes of small anomalies with less contrasts than the Gauss-Newton approach, but the values reconstructed using the Hessian-free approach are more stable against noise in data than the Gauss-Newton approach. That makes sense, because the approximations made for diagonalising the Hessian matrix, Eqs. (32) and (33), have had some regularisation effects on the reconstructed images. It must be reminded that the computational cost of the proposed Hessian-free inversion approach was almost an order of magnitude less than the Gauss-Newton approach because of solving each linearised subproblem in a single step.

7. DISCUSSION

This manuscript proposed a robust and low-cost approach for quantitative reconstruction of the sound speed from transmission ultrasound time series. It was shown that this inversion approach can reconstruct high-resolution and quantitatively accurate images of the sound speed for soft tissues. The proposed image reconstruction approach was tested on a realistic digital breast phantom [48]. Like the inversion approach proposed in [3], the propagation of acoustic waves is modelled using Green's formula which accounts for aberrations in phase and amplitude of the Green's function because of heterogeneity, refraction, geometrical spreading, and acoustic absorption and dispersion. For approximating the amplitude decay because of geometrical spreading, the changes in the area of ray tube is computed for each linked ray via solving an additional paraxial system of equations using the second part of Algorithm 1, as described in section 4. The proposed ray-based inversion approach reconstructed high-resolution images of the breast phantom via including the first-scattered waves in the image reconstruction. In experimental settings, a great portion of higher-scattered waves are attenuated because of acoustic absorption, or are buried in noise. The proposed inversion approach is an improvement to the prototype Born and distorted Born inversion approaches used for medical UST, because these approaches neglect the medium's heterogeneity in modelling the incident and scattered Green's functions, and the heterogeneity is included only in the scattering potential [18, 19, 20, 21, 36, 23, 25, 26]. However, figures 3(a) and 3(b) show that neglecting the acoustic heterogeneities in computing the Green's function has led to large errors in approximating phase and amplitude, respectively.

For solving the inverse problem, it was shown that the whole computational time for the Gauss-Newton inversion approach [3], which solves each linear subproblem via an implicit and iterative

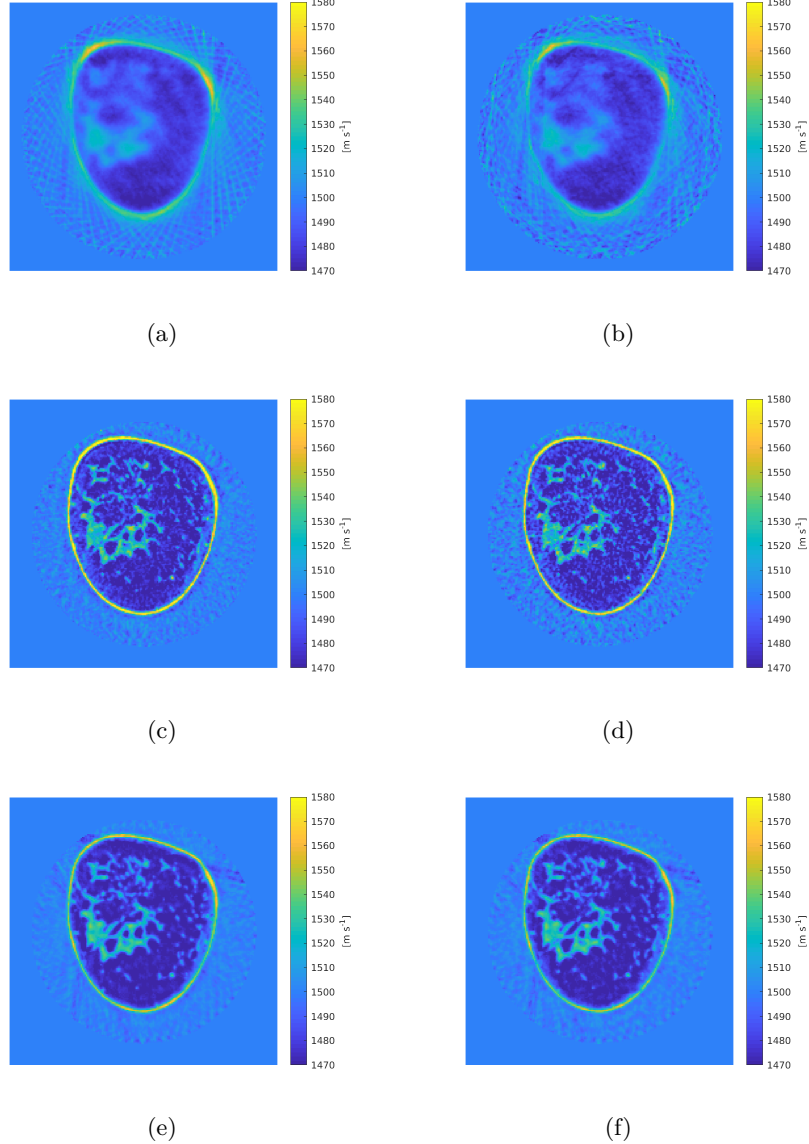


FIGURE 5. Reconstructed images using: time-of-flight-based approach (initial guess): (a) 30 dB, $RE = 76.64\%$, (b) 25 dB, $RE = 81.16\%$, Gauss-Newton: (c) 30 dB, $RE = 43.80\%$, (d) 25 dB, $RE = 51.04\%$, Hessian-free: (e) 30 dB, $RE = 44.78\%$, (f) 25 dB, $RE = 48.29\%$. The absorption coefficient map of the breast was assumed homogeneous and $\alpha_0 = 0.5 \text{ dBMHz}^{-y} \text{cm}^{-1}$.

inversion of the Hessian matrix, was almost the same as the computational time for simulating the breast-in-water synthetic data set using a prototype full-waveform approach [38], i.e., solving a single forward problem of the full-waveform inversion. To further reduce the computational cost, this study proposed a Hessian-free inversion approach, which is computationally about an order of magnitude faster than the Gauss-Newton inversion approach proposed in [3], because it solves the

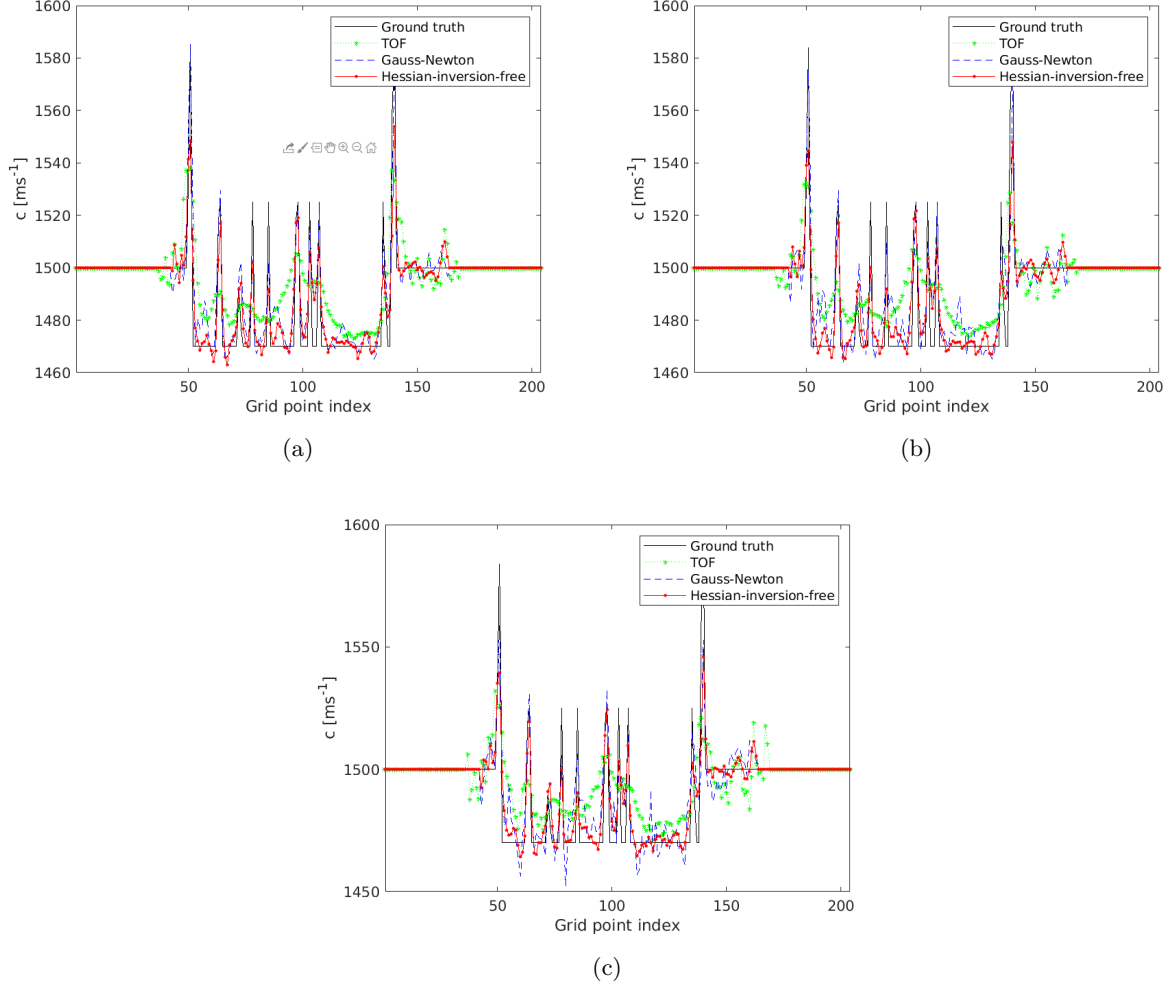


FIGURE 6. The reconstructed sound speed values on the main diagonal of the grid for image reconstruction from ultrasound data with: a) 40 dB SNR, b) 30 dB SNR, and c) 25 dB SNR. The absorption coefficient α_0 map of the breast was assumed homogeneous and $0.5 \text{ dBMHz}^{-y} \text{cm}^{-1}$.

linear subproblem associated with each frequency set in a single step and using (46) and (47). In addition, the proposed Hessian-free ray-born inversion approach was more stable than the Gauss-Newton approach to noise. For the UST data with 30 dB and 25 dB SNR, the proposed Hessian-free inversion approach reconstructed sound speed images with lower artefact than the Gauss-Newton inversion approach. In addition, the Hessian-free approach was more stable than the Gauss-Newton approach to changes in parameters of image reconstruction or initial guess.

The proposed forward model can account for acoustic absorption and dispersion via solving a lossy Helmholtz equation based on Szabo's wave model, but the acoustic absorption coefficient map is not known in practical settings. Accordingly, it was shown that the images reconstructed using an assumption of homogeneous absorption coefficient is comparable to the images reconstructed using

a true and known absorption coefficient map for the breast, but neglecting absorption has led to less accurate reconstructed images.

In general, ray-Born inversion approaches combine ray theory with Born approximation. The latter, which is based on a low-frequency approximation, assumes that for each emitter-receiver pair, scattered waves measured on the receiver can be affected by scatterings on any point in the medium. Instead, the inversion approach proposed in this study uses a high-frequency approximation, and assumes that waves are scattered in vicinity of a ray linking an associated emitter-receiver pair more likely than regions far away from this ray. While this assumption is not exact, it is a very good approximation for the frequency ranges used in the prototype ultrasound systems [4, 9].

In addition, the diagonalisation of the Hessian matrix is based on an assumption of an exact 2D Fourier integral of the Dirac delta function. However, because of partial coverage of $|\bar{\mathbf{k}}|$, the Fourier integral derived via weighting the Hessian matrix is not exact. The coverage of $|\bar{\mathbf{k}}|$ is partial, because the transducers are inherently band-limited. Therefore, because of the filtering enforced on the derived 2D Fourier integral in the polar coordinates of $\bar{\mathbf{k}}$, the associated inverse Fourier integral is a Dirac delta function which has been smoothed in space. As shown in the line plots in figures 6(a), 6(b) and 6(c), the filtered Fourier integral in frequency has led to slight smoothness and loss of contrast in the reconstructed images, but it significantly improved the stability of image reconstruction against noise in data, changes in initial guess or parameters of image reconstruction. (The latter was not shown.) It is expected that the spatial resolution and the contrast of images reconstructed using the Hessian-free approach, compared to the Gauss-Newton approach, be improved via using more broadband transducers.

The main motivation for developing the image reconstruction approach proposed in this study, and ray-based image reconstruction approaches developed in [3, 34], is for volumetric reconstruction of the sound speed from UST data measured in 3D settings, because acoustic waves inherently travel in three dimensions, not along a horizontal plane. There are some problems which have hampered application of full-waveform approaches for 3D UST. Despite their many well-known advantages, these kinds of methods have still limitations regarding handling computational cost and directivity of transducers for some specific 3D geometries and when size of transducers is finite. These limitations can be dealt with more straightforwardly using ray-based methods than full-waveform approaches.

Considering the fact that this study has used inherently different approaches for simulation of synthetic UST data as the benchmark and image reconstruction, it is very likely that the simulation experiments in this study can be extended to practical 2D and 3D settings.

DATA AND CODE AVAILABILITY STATEMENT

The Matlab codes that support the findings of this study, as well as studies [3] and [34], are publicly available via the GitHub link in [1]. The original k-Wave simulated ultrasound data, which were used as the benchmark for findings of this study can either be reproduced via the example scripts in [1], or downloaded via the Zenodo link in [2] and added to the associated path in the GitHub project.

APPENDIX-A. HOMOGENEOUS GREEN'S FUNCTION

Here, the Green's functions for homogeneous media are introduced. For a 2D homogeneous medium, the Green's function is in the form [3]

$$g_{0,2D}(\omega, \mathbf{x}, \mathbf{x}') \approx [8\pi\phi_0(\omega, \mathbf{x}, \mathbf{x}')]^{-1/2} \exp\left(i[\phi_0(\omega, \mathbf{x}, \mathbf{x}') + \pi/4]\right). \quad (67)$$

For a 3D homogeneous medium, the Green's function satisfies [3]

$$g_{0,3D}(\omega, \mathbf{x}, \mathbf{x}') = [4\pi|\mathbf{x} - \mathbf{x}'|]^{-1} \exp(i\phi_0(\omega, \mathbf{x}, \mathbf{x}')). \quad (68)$$

Here, $\phi_0 = k|\mathbf{x} - \mathbf{x}'|$ is the accumulated phase in water.

REFERENCES

- [1] Ashkan Javaherian, Ray-based quantitative ultrasound-tomography toolbox, 2022, <https://github.com/Ash1362/ray-based-quantitative-ultrasound-tomography/>
- [2] Ashkan Javaherian, Transmission ultrasound data simulated using the k-Wave toolbox as a benchmark for biomedical quantitative ultrasound tomography using a ray approximation to Green's function, 2023, <https://zenodo.org/records/7717290>
- [3] A. Javaherian and B. Cox, Ray-based inversion accounting for scattering for biomedical ultrasound tomography, *Inverse Problems* vol. 37, no.11, 115003, 2021.
- [4] N. Duric P. Littrup, L. Poulo, A. Babkin, R. Pevzner, E. Holsapple, O. Rama and C. Glide, Detection of breast cancer with ultrasound tomography: First results with the Computed Ultrasound Risk Evaluation (CURE) prototype, *Med. Phys.* vol. 34, no.2, 2007.
- [5] J. F. Synnevag, A. Austeng and S. Holm, Adaptive beamforming applied to medical ultrasound imaging, *IEEE transactions on ultrasonics, ferroelectrics, and frequency control*, Vol. 54, no. 8, pp. 1606-1613, 2007. DOI: 10.1109/TUFFC.2007.431.
- [6] T. Hopp, N. Ruiter, J. C. Bamber, N. Duric and K.W.A. van Dongen (Eds.) 2017 International Workshop on Medical Ultrasound Tomography, Speyer, Germany.
- [7] C. Li, N. Duric, P. Littrup and L. Huang, In-vivo breast sound speed imaging with ultrasound computed tomography, *Ultrasound in Med. & Biol.*, vol. 35, no. 10, pp. 1615–1628, 2009.
- [8] N. V. Ruiter, M. Zapf, T. Hopp, R. Dapp, E. Kretzek, M. Birk, B. Kohout, H. Gemmeke, 3D ultrasound computer tomography of the breast: A new era?, *European Journal of Radiology*, vol. 81, Supplement 1, pp. S133-S134, 2012.
- [9] H. Gemmeke, T. Hopp, M. Zapf, C. Kaiser, N.V. Ruiter, 3D Ultrasound Computer Tomography: Hardware Setup, Reconstruction Methods and First Clinical Results, *NUCL INSTRUM METH A*, vol. 873, 2017, pp. 59-65, 2017.
- [10] K. J. Opielinski, P. Pruchnicki, P. Szymanowski, W. K. Szepieniec, H. Szweda, E. Swis, M. Jozwik, M. Tenderenda and M. Bulkowskif, Multimodal ultrasound computer-assisted tomography: An approach to the recognition of breast lesions, *COMPUT MED IMAG GRAP* vol. 65,pp. 102–114, 2018.
- [11] C. Li, L. Huang, N. Duric, H. Zhang, and C. Rowe, An improved automatic time-of-flight picker for medical ultrasound tomography, *Ultrasonics.*, vol. 49, pp. 61-72, 2009.
- [12] G. Y. Sandhu, C. Li, O. Roy, S. Schmidt, and N. Duric, Frequency domain ultrasound waveform tomography: breast imaging using a ring transducer, *Phys. Med. Biol.*, Vol. 60, 5381–5398, 2015.
- [13] J. W. Wiskin, D. T. Borup, E. Iuanow, J. Klock, M. W. Lenox, 3-D Nonlinear Acoustic Inverse Scattering: Algorithm and Quantitative Results, *IEEE T ULTRASON FERR*, vol. 64, no. 3, 2017.
- [14] A. V. Goncharsky and S. Y. Romanov, Iterative methods for solving coefficient inverse problems of wave tomography in models with attenuation, *Inverse Problems*, vol. 33, pp. 025003, 2017.
- [15] S. Bernard , V. Monteiller , D. Komatitsch and P. Lasaygues, Ultrasonic computed tomography based on full-waveform inversion for bone quantitative imaging, *Phys. Med. Biol.* Vol. 62, pp. 7011–7035, 2017.
- [16] F. Faucher and O. Scherzer, Adjoint-state method for Hybridizable Discontinuous Galerkin discretization, application to the inverse acoustic wave problem, *Computer Methods in Applied Mechanics and Engineering*, Vol. 372, 2020.
- [17] F. Li, U. Villa, N. Duric and M. A. Anastasio, "A Forward Model Incorporating Elevation-Focused Transducer Properties for 3-D Full-Waveform Inversion in Ultrasound Computed Tomography," in *IEEE T-UFFC*, Vol. 70, no. 10, pp. 1339-1354, Oct. 2023, doi: 10.1109/TUFFC.2023.3313549.
- [18] A. J. Devaney, A filtered backpropagation algorithm for diffraction tomography, *Ultrason. Imag.*, vol. 4, pp. 336–350, 1982.
- [19] A. J. Devaney and M. L. Oristaglio, Inversion procedure for inverse scattering within the distorted-wave Born approximation, *Physical Review Letters*, vol. (51), no. 4, 1983.
- [20] W. B. Beydoun and A. Tarantola, First Born and Rytov approximations: Modelling and inversion conditions in a canonical example, *J. Acoust. Soc. Am.*, vol. 83, pp. 1045-1055, 1988.

- [21] D. T. Borup, S. A. Johnson, W. W. Kimz and M. J. Berggren, Nonperturbative Diffraction tomography via Gauss-Newton iteration applied to the scattering integral equation, *Ultrasonic Imaging*, vol. 14, pp. 69-85, 1992.
- [22] T.D. Mast, Aberration correction for time-domain ultrasound diffraction tomography, *J. Acoust. Soc. Am.*, vol. 112, No. 1, 2002.
- [23] F. Simonetti, L. Huang, N. Duric, and P. Littrup, Diffraction and coherence in breast ultrasound tomography: A study with a toroidal array, *Med. Phys.*, vol. 36, pp. 2955, 2009.
- [24] P. Müller, M. Schürmann, and J. Guck, ODTbrain: a Python library for full-view, dense diffraction tomography, *BMC Bioinformatics*, vol. 16, iss. 1, p. 1-9, 2015.
- [25] N. K. Martiartu, C. Boehm, A. Fichtner, 3-D Wave-Equation-Based Finite-Frequency Tomography for Ultrasound Computed Tomography, *IEEE Transactions on Ultrasonics, Ferroelectrics, and Frequency Control*, Vol. 67, no. 7, pp. 1332 - 1343, 2020.
- [26] Y. Fan and L. Ying, Solving inverse wave scattering with deep learning, *Annals of Mathematical Sciences and Applications*, Vol. 7, No. 1, pp. 23-48, 2022.
- [27] F. Faucher, C. Kirisits, M. Quellmalz, and O. Scherzer, and E. Setterqvist, Diffraction Tomography, Fourier Reconstruction, and Full Waveform Inversion, In Handbook of Mathematical Models and Algorithms in Computer Vision and Imaging, 2022, doi. 10.1007/978-3-030-03009-4.
- [28] P. Thierry, S. Operto, and G. Lambare, Fast 2-D ray+Born migration/inversion in complex media, *GEOPHYSICS*, Vol. 64, No. 1, pp. 162-181, 1999.
- [29] V. Červený, Seismic ray theory, Cambridge University Press. 2001.
- [30] P. Huthwaite and F. Simonetti, High-resolution imaging without iteration: a fast and robust method for breast ultrasound tomography, *J. Acoust. Soc. Am.*, vol. 130, no. 3, pp. 1721-34, 2011.
- [31] S. Jin, R. Madariaga, J. Virieux, and G. Lambaré, Two-dimensional asymptotic iterative elastic inversion, *Geophys. J. Internat.*, Vol. 108, No.2, pp. 575-588, 1992.
- [32] G. Lambare, J. Virieux, R. Madariaga, and S. Jin, Iterative asymptotic inversion in the acoustic approximation, *GEOPHYSICS*, Vol. 57. No. 9, pp. 1138-1154, 1992.
- [33] G. Lambare, S. Operto, P. Podvin, and P. Thierry, 3D ray+Born migration/inversion—Part 1: Theory, *GEOPHYSICS*, Vol. 68, No. 4, 2003.
- [34] A. Javaherian, F. Lucka and B. Cox, Refraction-corrected ray-based inversion for three-dimensional ultrasound tomography of the breast, *Inverse Problems*, vol. 36, 125010, 2020.
- [35] N. N. Bojarski, The k-space formulation of the scattering problem in the time domain, *J. Acous. Soc. Am.*, vol. 72, 1982, pp. 570-584.
- [36] T. D. Mast, L. P. Souriau, D. D. Liu, M. Tabei, A. I. Nachman, and R. C. Waag, A k-space method for large-scale models of wave propagation in tissue, *IEEE Trans. Ultrason. Ferroelectr. Freq. Control*, vol. 48, 2001, pp. 341-354.
- [37] M. Tabei, T. D. Mast, and R. C. Waag, A k-space method for coupled first-order acoustic propagation equations *J. Acoust. Soc. Am.* vol. 111, pp. 53-63, 2002.
- [38] B. E. Treeby and B. T. Cox, k-Wave: MATLAB toolbox for the simulation and reconstruction of photoacoustic wave fields *J. Biomed. Opt.* vol. 15, no. 2, 021314, 2010.
- [39] J. F. Kelly, R. J. McGough, and M. M. Meerschaert, Analytical time-domain Green's functions for power-law media, *J. Acoust. Soc. Am.*, vol. 124, no. 5, pp. 2861-2872, 2008.
- [40] T. L. Szabo, Time domain wave equations for lossy media obeying a frequency power law, *J. Acoust. Soc. Am.*, vol. 96, pp. 491-500, 1994.
- [41] M. Liebler, S. Ginter, T. Dreyer, and R. E. Riedlinger, “Full wave modeling of therapeutic ultrasound: Efficient time-domain implementation of the frequency power-law attenuation, *J. Acoust. Soc. Am.*, vol. 116, pp. 2742-2750, 2004.
- [42] Pierce A D 1981 Acoustics: An Introduction to its Physical Principles and Applications 3rd Edition (Berlin: Springer and ASA Press) (<https://doi.org/10.1007/978-3-030-11214-1>)
- [43] J.C. Butcher, The numerical analysis of ordinary differential equations. Runge–Kutta and general linear methods, Wiley, 1987.
- [44] E. Kreyszig, 1993 Advanced engineering mathematics. John Wiley & Sons, Inc., New York.
- [45] J. Virieux and V. Ferra Ray tracing in 3D complex isotropic media: An analysis of the problem, *GEOPHYSICS*, vol. 56, no. 12, pp. 2057-2069, 1991.
- [46] A. H. Anderson and A. C. Kak, Digital ray tracing in two-dimensional refractive fields, *J. Acoust. Soc. Am.*, vol. 72, pp. 1593-1606, 1982.

- [47] V. Červený, T. J. Moser, Ray propagator matrices in three-dimensional anisotropic inhomogeneous layered media, *Geophys. J. Int.* Vol. 168, pp. 593–604, 2007.
- [48] Y. Lou, W. Zhou, T. P. Matthews, C. M. Appleton and M. A. Anastasio, Generation of anatomically realistic numerical phantoms for photoacoustic and ultrasonic breast imaging, *J Biomed Opt.*, vol. 22, no. 4, pp. 041015, 2017.
- [49] B. Petrović and S. Parolai, Joint Convulsion of Building and Downhole strong-motion recordings: evidence for the seismic wavefield being radiated back into the shallow geological layers, *Bulletin of the Seismological Society of America*, Vol. 106, No. 4, pp. 1720–1732, 2016, doi: 10.1785/0120150326.
- [50] A. H. Anderson and A.C. Kak, Simultaneous algebraic reconstruction techniques (SART): A superior implementation of the ART algorithm, *Ultrasonic Imaging*, vol. 6, no. 1, pp. 81-94, 1984.